



University of Zagreb
FACULTY OF SCIENCE

Jelena Luetić

**Measurement of the cross section for
associated production of a W boson and
two b quarks with the CMS detector at
the Large Hadron Collider**

DOKTORSKI RAD

Zagreb, 2015.



University of Zagreb
FACULTY OF SCIENCE

Jelena Luetić

**Measurement of the cross section for
associated production of a W boson and
two b quarks with the CMS detector at
the Large Hadron Collider**

DOCTORAL THESIS

Supervisor: Professor Vuko Brigljević, PhD

Zagreb, 2015



Sveučilište u Zagrebu
PRIRODOSLOVNO MATEMATIČKI FAKULTET

Jelena Luetić

**Mjerenje udarnog presjeka zajedničke
produkциje W bozona i para b kvarkova
CMS detektorom na Velikom
hadronskom sudarivaču**

DOKTORSKI RAD

Mentor: Prof. dr. sc. Vuko Brigljević

Zagreb, 2015.

Doktorski rad izrađen je na Sveučilištu u Zagrebu Fakultetu elektrotehnike i računarstva,
na Zavodu za ...

Mentor: prof. dr. sc. Vuko Brigljević

Doktorski rad ima: XYZ stranica

Doktorski rad br.: _____

Contents

1. Theoretical overview	1
1.1. Standard model overview	1
1.1.1. Bottom quarks	3
1.1.2. Discovery and role of W boson	3
1.2. W + b jets at hadron colliders	4
1.2.1. Cross sections at hadron colliders	5
1.2.2. Contributions to Wbb cross section	9
1.3. Previous measurements	15
2. Large Hadron Collider	18
2.1. Physics goals for the LHC	18
2.2. Design of the LHC	20
2.3. Performance	22
3. Compact Muon Solenoid	24
3.1. CMS coordinate system	25
3.2. Solenoid magnet	25
3.3. Inner tracker system	26
3.3.1. Pixel Detector	26
3.3.2. Strip detector	26
3.4. Electromagnetic calorimeter	27
3.5. Hadronic calorimeter	28
3.6. Muon chambers	28
3.7. Trigger	29
4. Physics objects definitions	32
4.1. Electrons	32
4.1.1. Electron identification	32
4.2. Muons	34
4.2.1. Muon identification	34

4.3.	Lepton isolation	34
4.4.	Jets	35
4.4.1.	Jet algorithms	35
4.4.2.	Jet corrections	38
4.4.3.	Jet identification	38
4.4.4.	Jets from b quarks	39
4.5.	Missing transverse energy	41
5.	Event selection and analysis strategy	42
5.0.1.	Signal extraction	42
5.0.2.	Systematics	43
5.0.3.	Fit Results	44
5.0.4.	Tests of the fit stability	44
A.	Lorentz angle measurement in Pixel detector	47

Chapter 1

Theoretical overview

Standard model of elementary particles is a theory emerged in 1960s and 1970s describing all of the known elementary particles and interactions except gravity. The final formulation of Standard model incorporates several theories: quantum electrodynamics, Glashow-Weinberg-Salam theory of electroweak processes and quantum chromodynamics, all of them describing the relations between quarks and fermions. First steps towards formulation of Standard model occurred in 1960, when Sheldon Glashow unified electromagnetic and weak interactions. In 1967, Steven Weinberg and Abdul Salam are using Higgs mechanism in the electroweak theory explaining the origin of mass for elementary particles. After discovery of neutral currents which arise from the exchange of the neutral Z boson, electroweak theory becomes generally accepted. W and Z bosons were discovered in 1981 at CERN, and their masses were in agreement with the Standard model prediction. Theory describing strong interactions got its final form in 1974, when it was shown that hadrons are consisting of quarks. There are evidences which show the Standard model is not a final theory of elementary particles, but so far its predictions were confirmed every time through numerous experimental tests. Standard model has one additional nice property, all fundamental interactions arise from one general principle, the requirement of local gauge invariance.

In this chapter a brief overview of the standard model particles and interactions will be shown with the emphasis on the W boson and b quarks which are the most relevant for this thesis. Cross section determination at hadron colliders will be shown. In the last part of the chapter historical account of the development of W+b-jets theoretical calculations is described together with the existing experimental results.

1.1 Standard model overview

Elementary particle physics is described within a framework of standard model. We usually imagine particles as point like objects and some forces between them. Particles, or matter, are

fermions, leptons or quarks of spin $s = 1/2$. There are three charged leptons, electron, muon and tau which properties are the same except for their mass. Each of the leptons has a corresponding neutrally charged neutrino which has a very small mass. There are six different types of quarks with charge either $Q = 2/3$ or $Q = -1/3$. They also carry one additional quantum number which is color charge. All objects observed in nature are colorless giving raise to the concept of quark confinement. Colorless composite objects are classifies into two categories. Bayons are fermions which are made out of three quarks, for example proton or neutron. The other category are mesons which are made of two quarks like pions. Matter is divided into three categories which are identical except for the masses of the particles.

From the point of view of the quantum field theory, standard model is based on a gauge symmetry $SU(3)_C \times SU(2)_L \times U(1)_Y$. Strong interaction is described by $SU(3)_C$, while electroweak sector is described by $SU(2)_L \times U(1)_Y$. All interactions within Standard Model are mediated by an elementary particle which is a spin 1 boson. In the case of electromagnetic interaction, mediator is massless photon thus the range of electromagnetic interaction is infinite. For weak force mediators are three massive bosons W^\pm and Z and it's range is very small (10^{-16}). These four bosons are the gauge bosons of $SU(2)_L \times U(1)_Y$ group. The interaction between electroweak bosons is allowed in the Standard Model in a way that charge conservation principle remains valid. Strong force is mediated by the exchange of 8 massless gluons which are gauge bosons for $SU(3)_C$. Although gluons are massless, the range of the strong force is not infinite. Because of the effect of confinement, the range of the strong force is approximately the size of the lightest hadrons ($10^{-13}cm$).

Three generations of matter (fermions)			
	I	II	III
mass →	$2.4 \text{ MeV}/c^2$	$1.27 \text{ GeV}/c^2$	$171.2 \text{ GeV}/c^2$
charge →	$2/3$	$2/3$	$2/3$
spin →	$1/2$	$1/2$	$1/2$
name →	u up	c charm	t top
Quarks	d down	s strange	b bottom
	$4.8 \text{ MeV}/c^2$	$104 \text{ MeV}/c^2$	$4.2 \text{ GeV}/c^2$
	$-1/3$	$-1/3$	$-1/3$
	$1/2$	$1/2$	$1/2$
Leptons	e electron	ν_e electron neutrino	ν_τ tau neutrino
	$<2.2 \text{ eV}/c^2$	$<0.17 \text{ MeV}/c^2$	$<15.5 \text{ MeV}/c^2$
	0	0	0
	$1/2$	$1/2$	$1/2$
Gauge bosons	γ photon	Z^0 Z boson	W^\pm W boson
	0	91.2 GeV/c^2	80.4 GeV/c^2
	0	0	± 1
	1	1	1
	Higgs boson		
			? GeV/c^2
			0
			0
			0

Figure 1.1: List of Standard model elementary particles.

Scalar sector of the standard model has been experimentally confirmed only recently [1, 2]. The fact that weak gauge bosons are massive indicates that $SU(2)_L \times U(1)_Y$ is not a good

symmetry of the vacuum. In contrast with photon being massless, $U(1)_{em}$ is a good symmetry of the vacuum which means that $SU(2)_L \times U(1)_Y$ electroweak symmetry is somehow spontaneously broken to $U(1)_{em}$ of electromagnetism. Spontaneous symmetry breaking is implemented through Higgs mechanism which gives masses to W^\pm and Z boson, fermions and leaves photon massless. The details of the mechanism can be found elsewhere [3] but the main point is that the mechanism also predicts a new scalar and electrically neutral particle which is called Higgs boson. The search for Higgs boson lasted few decades before finally in 2012, a new particle was discovered with mass of 125 GeV. In subsequent years, properties of this new particle have been measured and at this point, all measurements agree with Standard Model predictions for Higgs boson.

1.1.1 Bottom quarks

Bottom quark was first predicted by Makoto Kobayashi and Toshihide Maskawa in 1974 when extending Cabibbo weak mixing angle to take into account CP violation observed in neutral K mesons. [4] The name "bottom" was introduced in 1975 by Haim Harari. The bottom quark was discovered in 1977 by the Fermilab E288 experiment team led by Leon M. Lederman through the observation of Υ resonance. [5] Kobayashi and Maskawa won the 2008 Nobel Prize in Physics for their explanation of CP-violation.

At the LHC, the main production mechanism for b quarks is through strong interaction ($g \rightarrow bb$) and top quark decay ($t \rightarrow Wb$). Every b quark, after production, goes through the process of hadronisation, forming one of the color neutral B mesons. B meson decays electromagnetically if produced in excited state to the ground state. Lowest state B mesons decay weakly, resulting in relatively long lifetime of 1.5 ps. According to CKM matrix 1.1, b quark can decay either to c quark ($\approx 95\%$ of the cases) or u quark ($\approx 95\%$ of the cases). Long lifetime of b quark makes it possible to traverse a substantial distance inside the detector. This fact is used in the creation of various b-tagging algorithms which are taking into account tracks originating from displaced vertices, discussed in Section 3.

$$\begin{pmatrix} V_{ud} & V_{us} & V_{ub} \\ V_{cd} & V_{cs} & V_{cb} \\ V_{td} & V_{ts} & V_{tb} \end{pmatrix} = \begin{pmatrix} 0.974 & 0.225 & 0.003 \\ 0.225 & 0.973 & 0.041 \\ 0.009 & 0.040 & 0.999 \end{pmatrix} \quad (1.1)$$

1.1.2 Discovery and role of W boson

W boson is one of the massive mediators of weak interaction with a mass of $m_W = 80.1$ GeV. The theory of the weak interactions got its final form in 1968 when Sheldon Glashow, Steven

Weinberg, and Abdus Salam unified a theory of electromagnetism and weak interactions. The discovery of W and Z bosons at UA1 and UA2 experiments was one of the major successes of the CERN experimental facility. Super Proton Synchrotron was the first accelerator powerful enough to produce W and Z bosons. Both collaborations reported their findings in 1983 [6, 7]. W boson at the LHC is primarily produced through quark-antiquark annihilation. In majority of the cases, W boson decays to quark-antiquark pair (66%). Other decay channels include creation a lepton and it's corresponding neutrino($\approx 10\%$ per lepton generation). This decay channel was the most important for W boson discovery and it's still essential for W boson detection at hadron colliders despite the large hadronic backgrounds.

Study of W+jets production at hadron colliders started in 1980s motivated by the top quark searches. Additional jets either come from radiation of additional quarks or gluons. However, because they carry color charge, quarks and gluons undergo the process of parton shower and hadronization forming jets in the detector. Parton shower is the process in which a high energy colored particle emits a low energy colored particle while hadronization is the process in which colored particle combine to form color neutral particles. Parton shower and hadronization cannot be computed analytically, but have to be modeled using Monte Carlo simulations. As a result of these processes, in the final state there can be a number of jets that doesn't correspond to the number of incoming partons. This becomes relevant when trying to form an inclusive W+jets sample from exclusive (W + 1 jet, W + 2 jets...) samples and some process of matching has to be performed in order to avoid double counting. Matching procedure is described in detail in [8].

Many theoretical issues arise when trying to compute cross sections for W+jets processes. Divergences while calculating amplitudes come from emission of soft particles or collinear jets. These problems are solved by introducing a cut-off called factorization scale. Other divergences come from integrating higher-order loops. Usually this type of divergence is than included into renormalized coupling constant. This procedure, however introduces a certain scale dependence into the result which will be discussed further in Section 1.2.1.

1.2 W + b jets at hadron colliders

First theoretical computations of W boson in association with b jets were published in 1993 [9], however only recently enough luminosity has been collected at hadron colliders to be able to make cross section measurements. This process was first interesting as a background to top quark searches and measurements where top quark decays to W boson and a b quark. In past few years, with the Higgs boson discovery, an important open question is whether the new particle also couples to fermions, and in particular to bottom quarks. Determination of this coupling requires direct measurement of the corresponding Higgs boson decay, as recently reported by

the CMS experiment in the study of Higgs decays to bottom quarks [10, 11]. Standard model Higgs boson branching ratio for decays into a bottom quark-antiquark pair (bb) is $\approx 58\%$. Study of this decay channel is therefore essential in determining the nature of the newly discovered boson. The measurement of the $H \rightarrow bb$ decay will be the first direct test of whether the observed boson interacts as expected with the quark sector, as the coupling to the top quark has only been tested through loop effects. However, the large backgrounds for this measurement make it essential that all the contributing processes including $W+b$ jets are well understood. There are also Beyond Standard Model searches where contributions from this process is substantial including some Supersymmetry searches with lepton, b jets and missing energy in the final state.

Soft and collinear divergences are naturally avoided in processes with b jets because of relatively high mass of b quark which means that the scale of the process doesn't go below $2m_b$.

1.2.1 Cross sections at hadron colliders

Determining cross sections for processes at hadron collides is not an easy task. With proton being a composite object consisting of partons, it is necessary to include it's internal structure as well as the diagrams for hard scattering of interest. This means soft and hard processes are occurring in the same event. Quarks and gluons within proton interact through strong force and are described using quantum chromodynamics. Two processes make it possible to perform calculations within the QCD, asymptotic freedom and factorization theorem. Since strong force coupling constant α_s depends on the scale, for high momentum transfers ($Q >> \Lambda_{QCD} \approx 200\text{MeV}$) it becomes sufficiently small to make perturbative expansion in α_s possible. This feature is called asymptotic freedom and it is used to determine the hard process cross section. Figure 1.2 shows the results of the α_s measurements which is in complete agreement with the QCD predictions of asymptotic freedom.

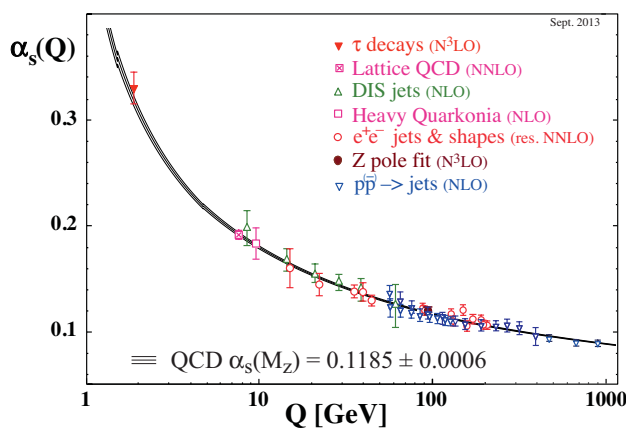


Figure 1.2: Summary of measurement of strong coupling constant α_s [12]

Perturbative QCD cannot be used if the momentum transfer values are small and the coupling constant becomes large. This phenomenon is called *confinement* and it requires different treatment for the quarks inside the proton. Internal structure of a proton is described using parton distribution functions which are determined through deep inelastic scattering experiments. Parton distribution functions for each of the partons inside a proton is shown in Figure 1.3 made with one specific PDF function(MSTW). Using DGLAP equations, it is possible to evolve the PDFs for any momentum transfer value which is described in detail in [13]

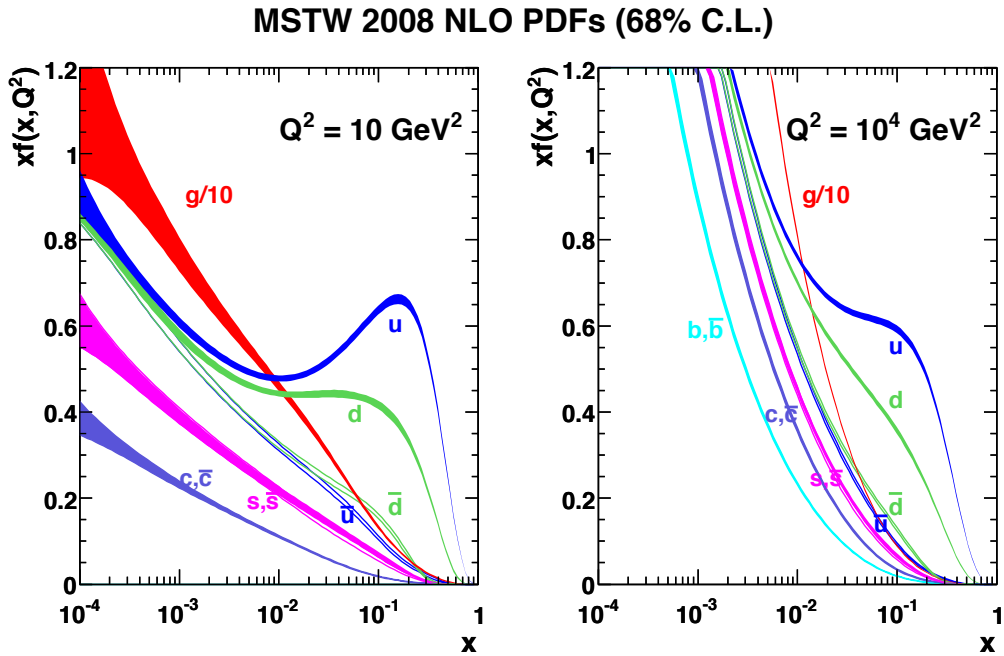


Figure 1.3: Parton distribution functions calculated by the MSTW group for $Q = 10\text{GeV}$ and $Q = 10^4\text{GeV}$ [14]

While performing perturbative QCD calculations, it is important to impose conditions to the final state in order to avoid soft and collinear divergences. Collinear divergences originate from configurations with a small opening angle between jets. Soft divergences appear when quark or gluon is irradiated at low momentum. Factorization scale is introduced as a cut-off for diagram calculation below which perturbative QCD calculation is not performed which means that hard scattering between partons is independent from the parton internal structure. The main point of the factorization theorem is that because of energy dependence of strong coupling constant, hard and soft part of the process are happening at different time scales and soft part is factorized inside a parton distribution function. Drawing of a proton proton collision is shown in figure 1.4. If we want to calculate the cross section for some process where there are two protons in the initial state and some interesting final state which we call X, according to [13], necessary steps are:

1. Identify the leading order partonic processes that contribute to X

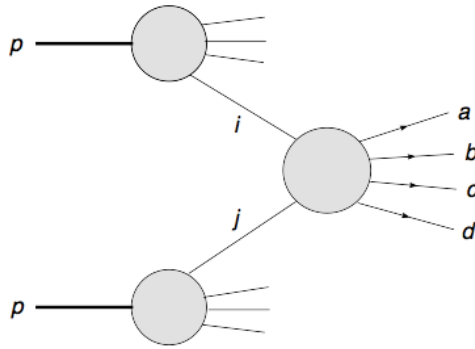


Figure 1.4: Drawing of a proton-proton collision.

2. Calculate the corresponding hard scattering cross section
3. Determine the appropriate PDFs for initial state partons
4. Make a specific choices for factorization(μ_F) and renormalization(μ_R) scales
5. Perform integration over the fraction of momentum available for a given parton(x)

The cross section at hadron collides is thus a convolution of the hard scattering perturbative cross section and two incoming parton distribution functions.

$$\sigma_{AB} = \sum_{n=1}^{\infty} \alpha_s^n(\mu_R^2) \sum_{i,j} \int dx_1 dx_2 f_{i/A}(x_1, \mu_F^2) f_{j/B}(x_2, \mu_F^2) \sigma_{ij \rightarrow X}^{(n)}(x_1 x_2 s, \mu_R^2, \mu_F^2) \quad (1.2)$$

Equation 1.2 shows cross section perturbation series in α_s , n denotes the order of the series where $n = 1$ is leading order, $n = 2$ is next to leading order, etc. Hard process cross section between two partons $\sigma_{ij \rightarrow X}^{(n)}$ is computed in the framework of perturbative QCD and depends on s which is squared center of mass energy. Two parton distribution functions are denoted with $f_{i/A}$ and $f_{j/B}$ and correspond to the probability density that parton $i(j)$ with proton momentum fraction $x_1(x_2)$ will be found inside a proton. Sum over all combinations of partons has to be computed. Integral over available phase space for proton fraction momentum dx is usually carried out by simulations.

Here μ_F represents *factorization scale* and μ_R is *renormalization scale* for running coupling constant. They are arbitrary cut-offs used to remove nonperturbative effects and be able to make perturbative calculations. If cross section is computed in full series, μ_F and μ_R should cancel out, and scale dependence should disappear. However, since fewer orders are used and some residual scale dependence is still present. This dependency can be used to estimate the contribution of the missing orders in the series.

Usually factorization and renormalization scales are chosen to be identical and close to the scale of the process in question.

NAPISATI PRIRODNE IZBORE SKALE!!!

Figure 1.5 shows some interesting Standard model cross sections in proton-proton and

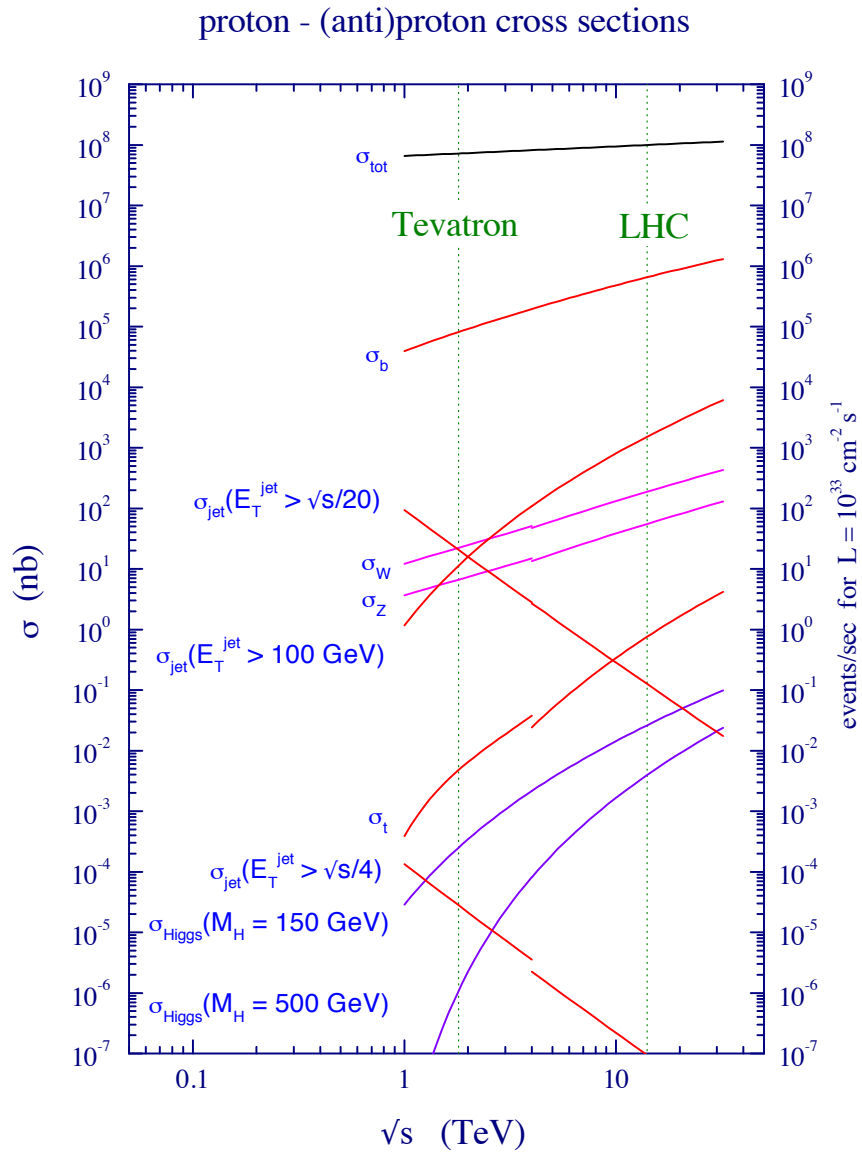


Figure 1.5: Standard model cross sections as a function of center of mass energy.[13]

proton-antiproton collisions as a function of a center of mass energy. All cross sections have been computed to the NLO order using the above described procedure.

1.2.2 Contributions to Wbb cross section

From theoretical point of view, calculations of W+b jets processes can be divided into two categories: only light quarks in the initial state shown in figure 1.6 (four flavour scheme - 4FS) and b quark in the initial state, usually called five flavor scheme (5FS) shown in Figure 1.9. Additional contribution to Wbb production at hadron colliders comes from double parton interactions where a W boson and a pair of b quarks is produced in different hard process inside the same collision as shown in Figure 1.10. This contribution will be discussed in Section 1.2.2.

The rationale behind using 4FS or 5FS is discussed in detail in [15]. Four flavor scheme approach assumes that bottom quarks are heavy and can only be created as pairs in collisions with high momentum transfer or as a decay product of t quark. Heavy quarks are not included in the initial state and their parton distribution function is set to zero which means an effective theory is created where heavy quarks do not enter the computation of running coupling and the evolution of PDFs. In this approach, it is assumed that scale is of the same order as the other hard scales in the process. If it happens that the scale of the process is much higher than the mass of the b quark, for example in the production of massive bosons, large logarithms of the type $\log(Q^2/m_b^2)$ appear and can spoil the convergence of a fixed order perturbative expansion and it introduces large scale dependence into the final result. In five flavor schemes calculations include b quark in the initial state which means some new and simpler processes become available. These calculation allow resummation of possibly large logarithms of type $\log(Q^2/m_b^2)$ into the b quark parton distributions function possibly transforming some higher order calculations into much simpler leading order calculations. The result in [15] shows that at the LHC 4-flavor calculations are well behaved and two schemes are in good agreement. The typical size of the possibly problematic logarithms in four flavor scheme in hadron colliders is not large enough to spoil convergence. On the other hand, five flavor scheme is less dependent on the scale of the process and show smaller uncertainties which is in general very good for predictions of inclusive observables.

First leading order calculations for associated production of a W boson and heavy quarks at hadron colliders were presented in 1993. Feynmann diagram for leading order W + 2 b jets production is shown in Figure 1.6. Exact leading order matrix element has been computed and higher order corrections were estimated using Monte Carlo. Their results are summarized in the Figure 1.7 where the differential cross section for W+2 b jets as a function of a leading b jet p_T is shown. Two scale choices have been studied, first one with $\mu_0 = M_{bb}$ which is the invariant mass of the dijet system and is represented with solid line. Second choice is $\mu_0 = m_W + p_T^W$ and is represented with the dotted line. Looking at the normalizations of two diagrams, the difference

is clearly visible which indicates a strong total cross section scale dependence. However, the shape of the differential cross section shows the same behavior in both cases which means that the scale only affects total cross section.

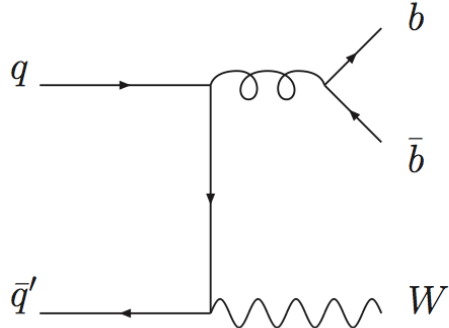


Figure 1.6: Leading order Wbb Feynmann diagram

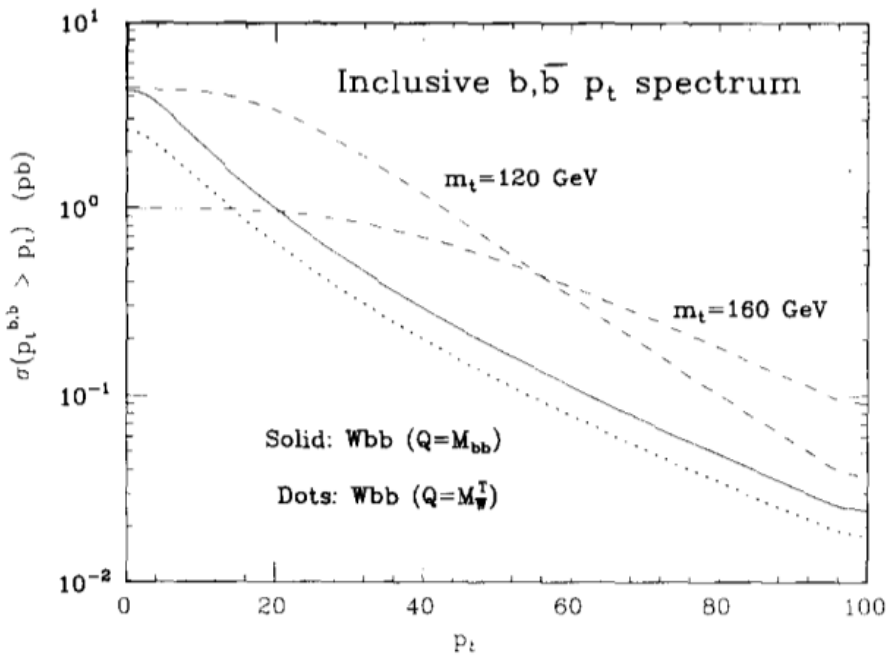


Figure 1.7: Scale dependence of Wbb cross section

Later development of theoretical calculations was strongly motivated by reducing the scale dependence of the result and it included adding additional partons to the final state. This was a first step towards the full NLO calculation. The only thing missing was taking into account the loop effects. This approach made it possible to access some previously inaccessible kinematics, however at the expense of introducing additional scale dependence. The list of new final states is simple and it includes $Wbbq$, $Wbbq\bar{q}$, $Wbb\bar{q}q'\bar{q}'\dots$. For the measurements at the LHC in particular, calculations for new initial states qg and gg were of great importance. First results

for W+2 jets were published in [16]. Additional calculations were shown in [17] for up to six additional jets in the final state. Although these processes are suppressed by an additional α_s factor, the gluon PDF inside a proton is much larger than anti-quark, so this production mechanism is significant at the LHC energies.

First full NLO calculations were published in 2006[18]. Events with b jet pair in the final state were selected, with momentum of the dijet system $p_T > 15$ GeV and a pseudorapidity less than 2. The results were shown for two categories, inclusive and exclusive, depending on the treatment of extra jets. In the inclusive case events with additional jets were included, while in the exclusive case exactly two jets were required. Figure 1.8 shows the overall scale dependence of LO, NLO inclusive and NLO exclusive total cross-sections, when both renormalization scale and factorization scale are varied independently between $\mu_0/2$ and $4\mu_0$ (with $\mu_0 = m_b + M_W/2$), including full bottom-quark mass effects. NLO cross sections have a reduced scale dependence over most of the range of scales shown, and the exclusive NLO cross-section is more stable than the inclusive one especially at low scales. This is consistent with the fact that the inclusive NLO cross-section integrates over the entire phase space of the $qg(\bar{q}g) \rightarrow b\bar{b}W + q(\bar{q})$ channels that are evaluated with NLO α_s and NLO PDF, but are actually tree-level processes and retain therefore a strong scale dependence. The effect of the b quark mass has been shown to affect the total NLO cross section on the order of $\approx 8\%$. This is expected to be small when considering well separated jets.

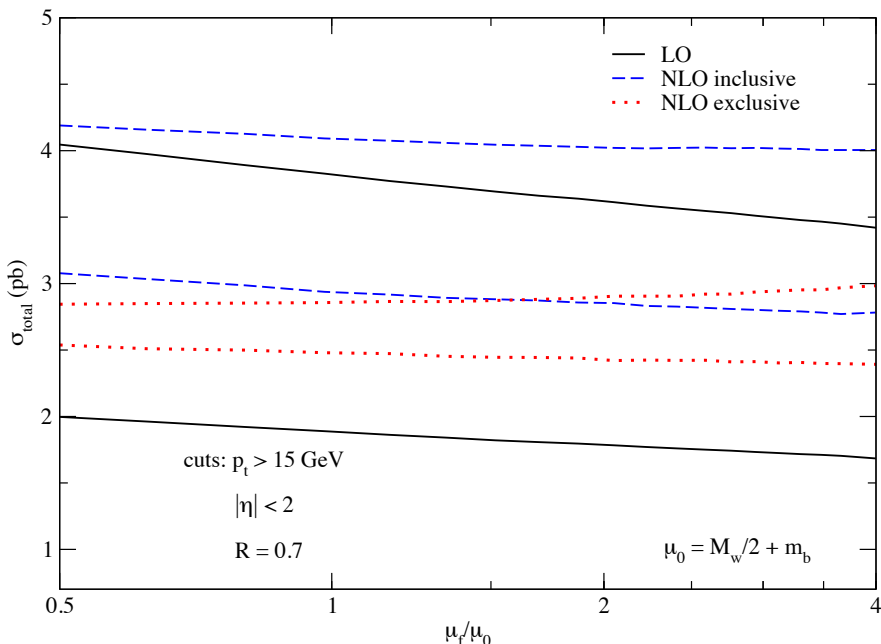


Figure 1.8: Wbb NLO scale dependence[18]

New results published in 2007 explored in particular NLO corrections for events with W boson and two jets where at least one is b-tagged. It was shown that for LHC the correction

factor is ≈ 1.9 . This paper was interesting in particular for its study of soft and collinear topologies, where two b quarks merge into one. Additionally, b quark in the initial state was considered giving rise to the processes like $bq \rightarrow Wbq'$ shown in figure 1.9. Parton distribution function for b quark needed to be determined perturbatively using DGLAP equations. Other approach is to consider a gluon in the initial state which then splits to $b\bar{b}$.

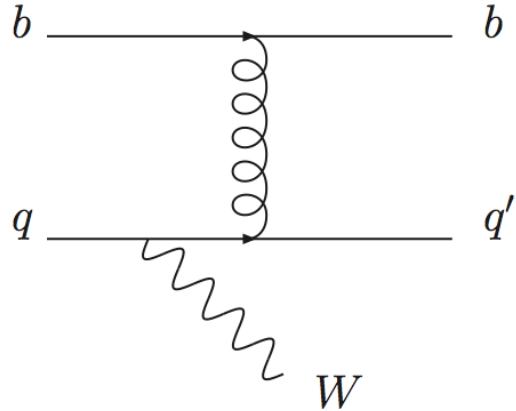


Figure 1.9: Wbb production within 5 flavor scheme

Double parton scattering

Multiple parton interactions happen due to composite nature of the proton. Usually inside a proton, only one parton has significant fraction of proton momentum x to produce a hard scattering. However, sometimes can happen that two such partons exist which results in two hard scatterings in the same collision. This phenomenon is called Double Parton Scattering (DPS) and is shown in Figure 1.10. In the framework of this thesis, this means that two partons are responsible for creation of a W boson and other two for creation of pair of b jets.

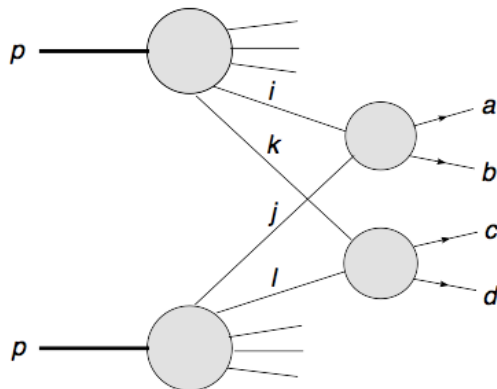


Figure 1.10: Double parton scattering

Double parton scattering cannot be modeled in the framework of perturbative QCD, but

it is approximated using simulations. The phenomenology of DPS starts from the assumption that factorization between two hard processes is possible, as well as factorization between hard processes and proton kinematics. Cross sections for hard scatterings are computed separately of each pair of partons. However, instead of using regular parton distribution functions, a new set of distribution functions has been defined which are called Double Parton Distribution Functions (dPDFs). Factorized cross section for two hard processes A and B to happen in proton-proton scattering can be written as:

$$\sigma_{(A,B)}^{DPS} \sim \sum_{i,j,k,l} \int dx_1 dx_2 dx'_1 dx'_2 d^2 b \Gamma_{ij}(x_1, x_2, b; Q_1, Q_2) \sigma_{ik}^A(x_1, x'_1) \sigma_{jl}^B(x_2, x'_2) \Gamma_{kl}(x'_1, x'_2, b; Q_1, Q_2) \quad (1.3)$$

Parton level cross sections are denoted with σ_{ik} , for hard process between partons i and k , and σ_{jl} for hard process between partons j and l . These are the same as for single parton scattering and are known for most of the processes of interest today. Quantity $\Gamma_{ij}(x_1, x_2, b; t_1, t_2)$ represents double parton distribution function which describes the probability of finding a parton i with momentum fraction x_1 at scale Q_1 inside a proton together with a parton j with momentum fraction x_2 at scale Q_2 . Another parameter in this distribution function is b which describes transverse distance between two partons. Scales Q_1 and Q_2 correspond to characteristic scales of hard processes A and B . For example in the framework of this thesis W boson production would correspond to process A and production of two b jets would correspond to process B . This study is described in detail in [19]. Usually, it is assumed that $\Gamma_{ij}(x_1, x_2, b; t_1, t_2)$ can be decomposed into two components, longitudinal and transversal in the following way:

$$\Gamma_{ij}(x_1, x_2, b; t_1, t_2) = D_h^{ij}(x_1, x_2; t_1, t_2) F_j^i(b) \quad (1.4)$$

The interpretation of the function $D_h^{ij}(x_1, x_2; t_1, t_2)$ within QCD is the probability of finding parton i with scale Q_1 and parton j with scale Q_2 . These functions cannot be determined using perturbative QCD, thus good modeling and to correctly take into account correlations between longitudinal momenta and transverse position is essential to making accurate cross section predictions.

More details on how to determine dPDFs can be found in [20], but in the simplest case $D_h^{ij}(x_1, x_2; t_1, t_2)$ can be taken as a product of single parton distribution functions taking into account effects like $x_1 + x_2 < 1$. Since $F_j^i(b)$ is the only part of $\sigma_{(A,B)}^{DPS}$ that depends only on b , integration over b can be performed giving an effective cross section σ_{eff} which is related to the size of the proton and can be seen as an effective area of the interaction. This approach

yields a simplified expression for the double parton scattering cross section:

$$\sigma_{(A,B)}^{DPS} \sim \frac{1}{\sigma_{eff}} \sigma_{(A)}^{SPS} \sigma_{(B)}^{SPS} \quad (1.5)$$

Here $\sigma_{(A)}^{SPS}$ and $\sigma_{(B)}^{SPS}$ are single parton scattering cross section which can be obtained using equation 1.2.

However, this factorized approach does not take into account some simple correlations like how finding a quark of some flavor affects the probability of finding another quark with the same flavor. While for some simple cases with low parton momentum fractions this factorized approach may give accurate results, for more complicated cases like calculating fiducial cross sections, acceptance cuts can spoil the equation. Thus, a simulation of the full kinematical effects is necessary.

First measurements of σ_{eff} have been performed by the AFS collaboration at the ISR (CERN) which was $\sigma_{eff} \sim 5$ mb at 63GeV. Both CDF and D0 collaborations at Tevatron reported $\sigma_{eff} \sim 15$ mb which is roughly 20% of the total $p\bar{p}$ cross section at Tevatron energies. Their data also shows no sign of dependence on x in their measured σ_{eff} in the x ranges accessible. Later measurements performed by ATLAS and CMS collaborations are in reasonable agreement with previous results. All results are summarized in Figure 1.11.

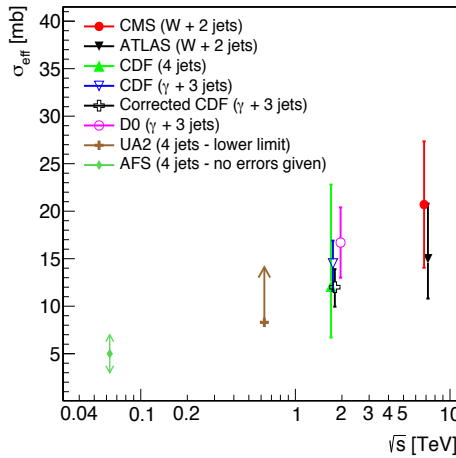


Figure 1.11: Center of mass energy dependence of σ_{eff} as reported from different collaborations. All these measurements use different approaches to estimate σ_{eff} . [21]

Double parton scattering measurement at CMS is performed by selecting the events with a W + 2-jet final state where one hard interaction produces a W boson and another produces a dijet [22]. The W + 2-jet process is attractive because the muonic decay of the W provides a clean tag and the large dijet production cross section increases the probability of observing DPS. Events containing a W + 2-jet final state originating from single parton scattering (SPS) constitute an irreducible background. Results were obtained by performing a template fit to two uncorrelated variables: the relative p_T balance between two jets (Δp_T) and the angle between

W boson and a dijet system. Obtained results again show that contribution of DPS to total cross section is $\sim 20\%$ which is in good agreement with previous Tevatron results. The DPS contribution in the case of W + 2 b jets is estimated to be $\sim 15\%$. [23]

1.3 Previous measurements

Previous measurements of a W boson produced in association with b quarks have been performed on different experiments. However, the final states and phase space used in these measurements were different, which means that the results cannot be directly compared, but they can be compared with theoretical predictions. This process was measured for the first time at Tevatron with D0 and CDF experiments at $\sqrt{s} = 1.96$ TeV. The CDF collaboration published its result in 2009 and the cross-section measured is that of “jets from b-quarks produced with a W boson”[24]. The event selection is based on reconstructing a leptonically decaying W boson, and one or two jets where at least one has to be b-tagged. Events with jets from light quarks are vetoed with a cut on the secondary vertex mass. Contribution of other background events containing a b quark in final state (e.g. events with top quark) is estimated using Monte Carlo simulations. The measured cross section is 2.8 standard deviations higher than corresponding theoretical prediction.

D0 collaboration published their result in 2012. with somewhat different phase space definition[25]. The difference with respect to the CDF measurement consists in the inclusion of the events with 3 jets and reduced pseudorapidity range in which the measurement was performed. The measurement technique is similar to that of CDF, although b-tagging algorithms were slightly different. The measured cross section was in good agreement with the Standard model prediction.

First measurements at the LHC were published by the ATLAS collaboration based on 36/pb of integrated luminosity at $\sqrt{s} = 7$ TeV. One year later they improved their measurement using 4.6/fb [26]. Selected events contain one reconstructed electron or muon, significant amount of missing transverse energy and one or two jets where exactly one is b-tagged. The phase space is divided in two regions, depending on the number of jets. Events with exactly 2 b jets and events with more than 2 jets are vetoed in order to suppress background events from top quark decay. The results are shown in Figure 1.12. The cross section measurement in the one jet region shows an excess corresponding to 1.5 standard deviations. In the two jet region, the measured cross section is in good agreement with theoretical predictions. A differential cross section measurement as a function of leading b jet transverse momentum has been performed for the first time and shown in figure 1.13. The cross section measurement in the one jet region is again higher than NLO predictions but within theoretical and experimental uncertainties. The cross section measured for the events with two jets is in good agreement with the theoretical

prediction. The CMS collaboration published its results corresponding to data collected during

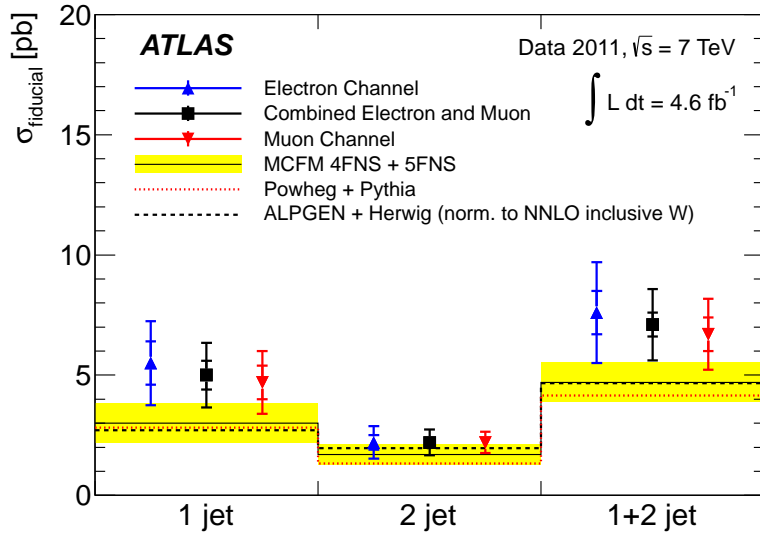


Figure 1.12: Measured fiducial cross-sections in the electron, muon, and combined electron and muon channels. The cross-sections are given in the 1-jet, 2-jet, and 1+2-jet fiducial regions.[26]

2011. The measured events contained a muon and missing transverse energy in the final state, together with two b-tagged jets. The measured cross section is in excellent agreement with the Standard model prediction.[23]

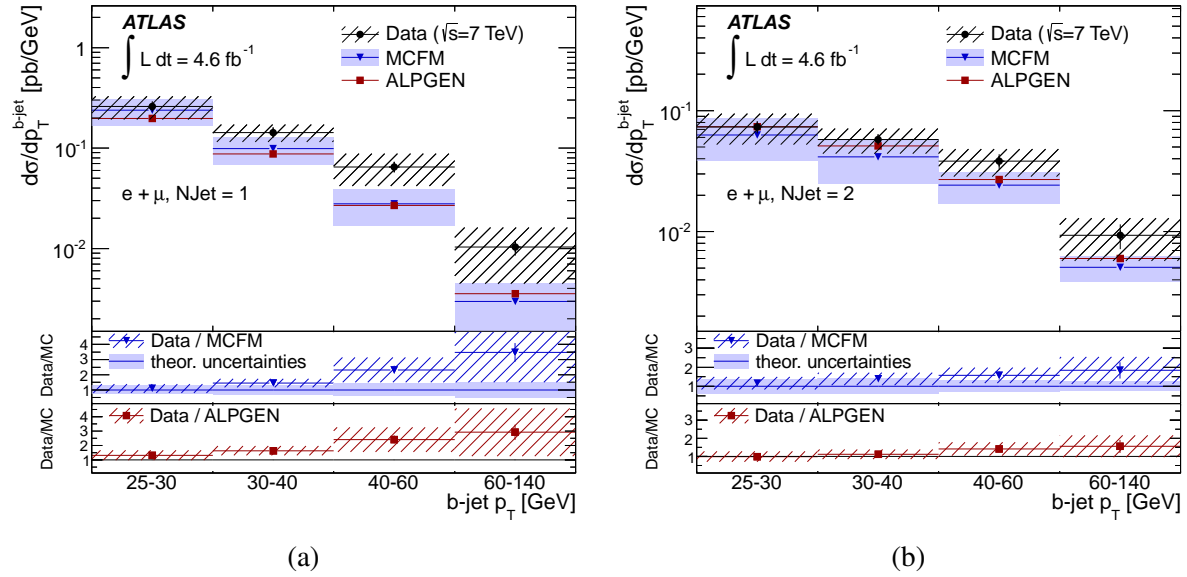


Figure 1.13: Measured differential W+b-jets cross-sections as a function of leading b-jet p_T in the 1-jet (1.13a) and 2-jet (1.13b) fiducial regions, obtained by combining the muon and electron channel results. [26]

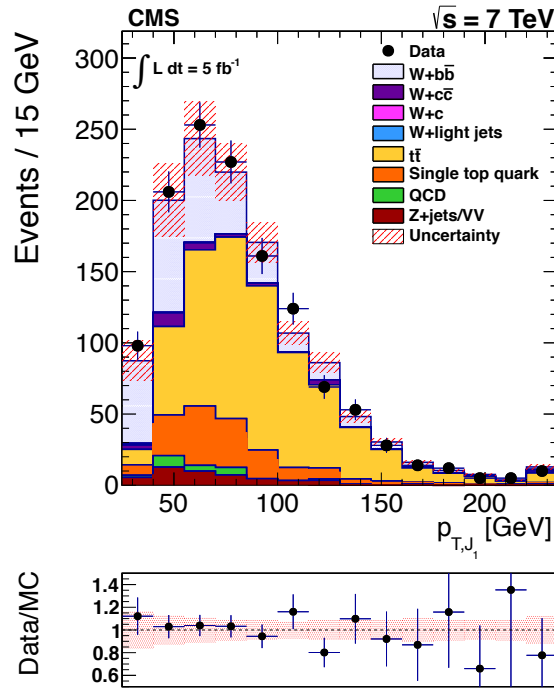


Figure 1.14: CMS Wbb total cross section measurement[23]

Chapter 2

Large Hadron Collider

CERN is the largest particle physics laboratory in the world, located near the city of Genava, on the French-Swiss border. It was founded in 1953 by 12 countries and today it has 21 member states. Its main function is to provide particle accelerators and infrastructure for high energy physics experiments. Current accelerator complex is a chain of smaller accelerators with increasingly higher energies of which the largest one is Large Hadron Collider (LHC) (Figure 2.1). Protons accelerated in the chain are obtained by taking hydrogen atoms and stripping them of the orbiting electrons. Protons are then accelerated by a small linear accelerator Linac2 to 50 MeV and injected to PS Booster. After reaching 1.4 GeV, protons are injected to Proton Synchrotron and accelerated to 25 GeV. Next accelerators in chain are Super Proton Synchrotron (SPS) with energy of 450 GeV, and Large Hadron Collider with beam energy of 7 TeV. In addition to proton-proton collisions, LHC is also able to deliver lead-lead collisions and lead-proton collisions. Some of the major physics results at CERN include the discovery of neutral currents, discovery of W and Z bosons, creation of antihydrogen atom and direct observation of CP violation among others. In this chapter, we will briefly go through the motivation for the LHC design, building blocks of the LHC will be presented together with the accelerator performance during the past few years.

2.1 Physics goals for the LHC

The standard model of elementary particles describes nicely all known particles and interactions, however there are still some unanswered questions. One of the major question was the existence of Higgs boson which was solved in the past few years with the discovery of a new particle at 125 GeV. In order to be able to claim a discovery, all known standard model processes have to be well measured and understood. This requirement lead to many precision measurements which determined precisely cross sections, couplings, masses and other parameters within the standard model. Any deviation from standard model predictions can be an evidence

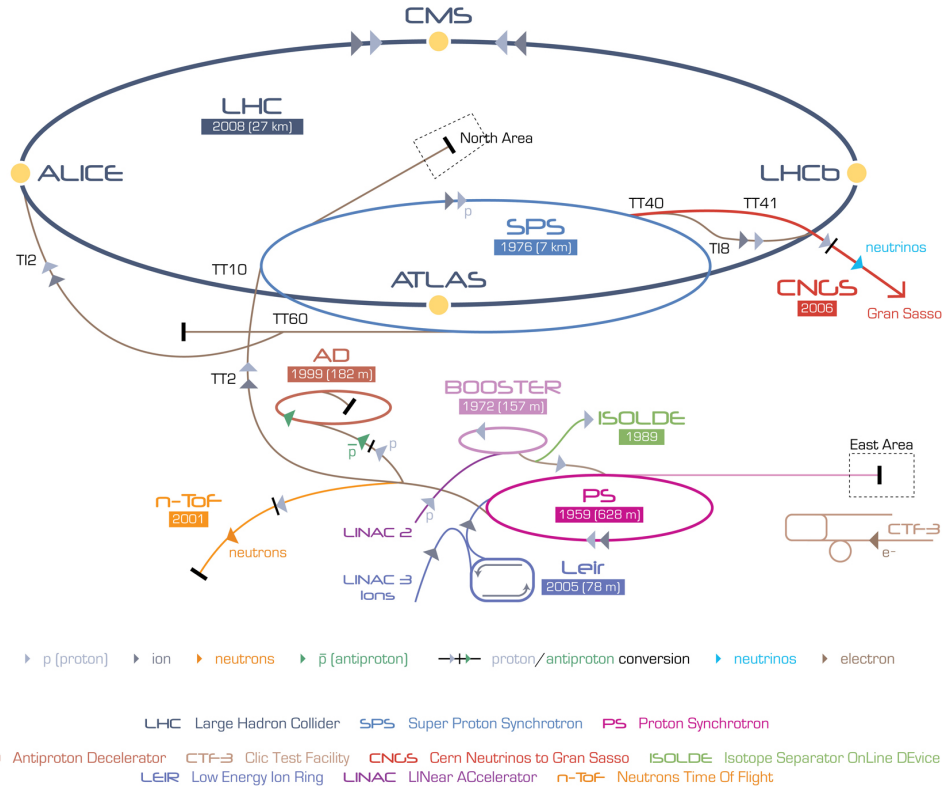


Figure 2.1: Schematics of Large Hadron Collider

for physics beyond standard model. One of the questions that remain open is the unification of fundamental forces, as it is difficult to construct a theory of gravity which would be similar to those of other fundamental interactions. One attempt to achieve this goal is the theory of supersymmetry which predicts that each particle has its heavier supersymmetric partner which according to some theories could unify all fundamental forces. If the theory of supersymmetry is correct, lightest supersymmetric particles could be found at the LHC. This could potentially solve the problem of the dark matter which could be, according to some theories, undiscovered supersymmetric particles. Also the problem of matter-antimatter asymmetry could be addressed trying to discover why is the world built only of matter. Other theories that involve extra dimensions, bound states of quarks and leptons LHC also performed lead-lead and lead-proton collisions in which a state called quark-gluon plasma is produced that resembles the conditions in the early universe.

During the past few years, various models for new physics have been extensively tested, and new exclusion limits have been set. After three years of data taking at 7 and 8 TeV, and a shutdown period of two years, LHC is now almost ready to deliver collisions at record energies of 13 TeV which could hopefully show signs of new physics.

2.2 Design of the LHC

The LHC is placed inside a 27 km tunnel, which lies between 45 m and 170 m below the ground surface and previously housed LEP accelerator. Beams circulating inside the LHC, collide at four interaction points. At each of these points, a detector has been built to record the products of proton collisions. This thesis uses data collected by the CMS (Compact Muon Solenoid) detector [27]. Other detector with the same purpose but different design is the ATLAS (A Toroidal LHC Apparatus) detector located at the opposite side of the LHC ring [28]. These two are so called multiple purpose particle detectors, covering a large portion of spacial angle around the interaction point, and aimed towards discovering Higgs boson, supersymmetry, precision measurements etc. The other two experiments are ALICE (A Large Ion Collider Experiment) which is designed to study quark-gluon plasma from lead collisions [29], and LHCb (LHC Beauty) for B physics [30]. Two other experiments TOTEM and LHCf are placed away from the interaction point to measure the products along the beam direction.

The LHC is made out of nearly 9600 different magnets, including dipoles, quadrupoles, sextupoles, octupoles, etc. The biggest ones are dipoles and there are 1232 of them. The magnets are made with superconducting niobium-titanium (NbTi) cables which go into a superconductive state at 9.2K. In order to achieve superconductivity and be able to withstand high currents (11850 A), cables have to be cooled with superfluid helium to less than 2K. Large magnetic fields in dipoles of 8.2T bend the proton beams around the ring. Other higher order magnets are used to focus and correct the beam. LHC magnets are designed in a way that both proton beams are counter-circulating inside a single cryogenic structure which requires oppositely magnetic field for each of the beams in order to be steered along the same circumference. One of the LHC magnets is shown in Figure 2.2 together with the drawing of the magnetic field inside the dipole.

Acceleration inside the LHC is provided by the radio frequency superconducting cavities (RF). It takes approximately 20 minutes for the beams to be accelerated from the injection at 450 GeV to full beam energy. RF chambers also provide a small corrections of the order of ~ 7 keV per turn to the beam due to the energy loss from synchrotron radiation.

Beams in the LHC are injected in series of bunches, with each bunch having more than 10^{11} protons. Bunches are arranged in trains of 72 bunches with 25 ns spacing between them and 12 empty bunches between trains. Peak collision rate of 40 MHz is achieved when collisions happen at every bunch crossing. Beams are squeezed to a transverse size of $\sim 17 \mu\text{m}$ at the interaction point in order to maximize the probability of collision.

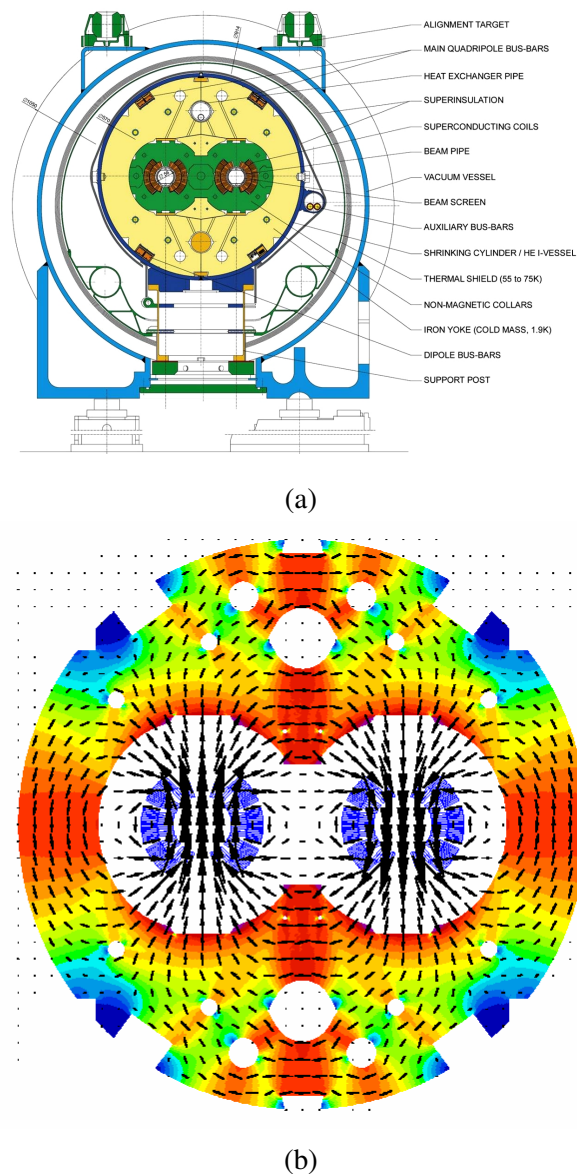


Figure 2.2: Schematics of Dipole magnets [31, 32]

2.3 Performance

Since the start of the LHC in 2009, there were three years of machine operation, which yielded many physics results among which the discovery of Higgs boson reported by ATLAS and CMS collaborations. should be highlighted. First year of operation was devoted to commissioning and understanding machine characteristics with the emphasis on safety and testing machine protection systems. In 2011 new energy and instantaneous luminosity records were reached. These numbers were increased once again in 2012 with center of mass energy going to 8 TeV.

High bunch intensity with 50 ns bunch spacing was used in order to get a good instantaneous luminosity performance. This came at a cost of high number of collisions in one bunch crossing (pile-up) which was in 2012 around 12 collisions, and in some cases this number went as high as 20 interactions. With the increase of instantaneous luminosity in 2012, number of pile-up interactions was on the average around 30. Besides proton-proton collisions, LHC successfully delivered lead-lead ion runs in 2010 and 2011. primarily for the ALICE experiment, but also for CMS and ATLAS. At the start of 2013. there was also a successful proton-lead run performed for the first time. LHC design parameters together with the 2012 operations parameters are shown in Table 2.1

Table 2.1: LHC performance in 2012 together with design performance[31]

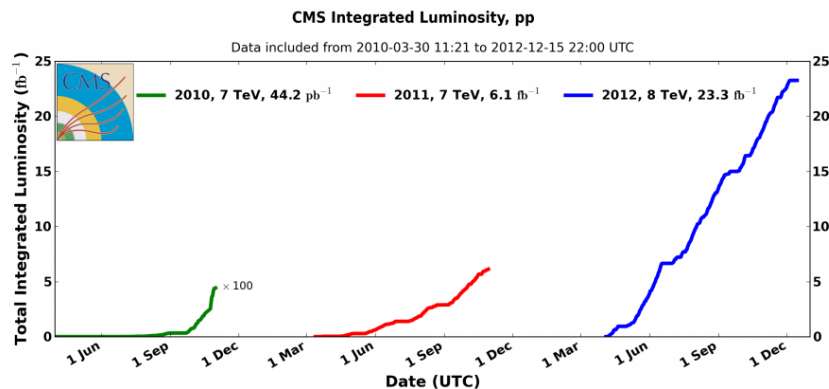
Parameter	Design value	Value in 2012
Beam energy [TeV]	7	4
Bunch spacing [ns]	25	50
Number of bunches	2808	1374
Protons per bunch	1.15×10^{11}	$1.6-1.7 \times 10^{11}$
Peak luminosity [$\text{cm}^{-2}\text{s}^{-1}$]	1×10^{34}	7.7×10^{33}
Max. number of events per bunch crossing	19	≈ 40
Stored beam energy [MJ]	362	≈ 140

LHC achieved very good luminosity performance during past years mainly because of the excellent beam quality delivered by the injectors with significantly more protons than nominal and with lower emittances. Since the LHC was capable to absorb these beams, it was chosen to continue to operate with 50 ns bunch spacing. This meant higher pile-up which had to be dealt with by the experiments. Some of the highlights of Run 1 operation are shown in Table 2.2.

Following a two year shutdown, LHC is anticipating operations at even higher energies of 6.5 TeV and later 7 TeV. The long term plan includes even higher peak luminosities, installation of the new injector complex and later the beginning of HL-LHC era. The timeline will, of course, be highly affected by the performance and results of the next run.

Table 2.2: LHC performance highlights

Max. luminosity delivered in one fill	237 pb^{-1}
Max. luminosity delivered in 7 days	1.35 fb^{-1}
Longest time in stable beams (2012)	22.8 hours
Longest time in stable beams over 7 days	91.8 hours (55%)

**Figure 2.3:** Luminosity delivered to the CMS experiment

Chapter 3

Compact Muon Solenoid

Compact Muon Solenoid is a general purpose detector designed to be able to cover a wide range of physics at the LHC. It has a layered design with each layer detecting different kinds of particles and covering a large portion or the spherical angle around the interaction point. Inside a large solenoid, with a tracker and calorimeter built inside to improve the resolution of the momentum measurements. Detectors outside the solenoid are designed primarily to detect muons.

DODATI JOS OPCENITO O CMS-u

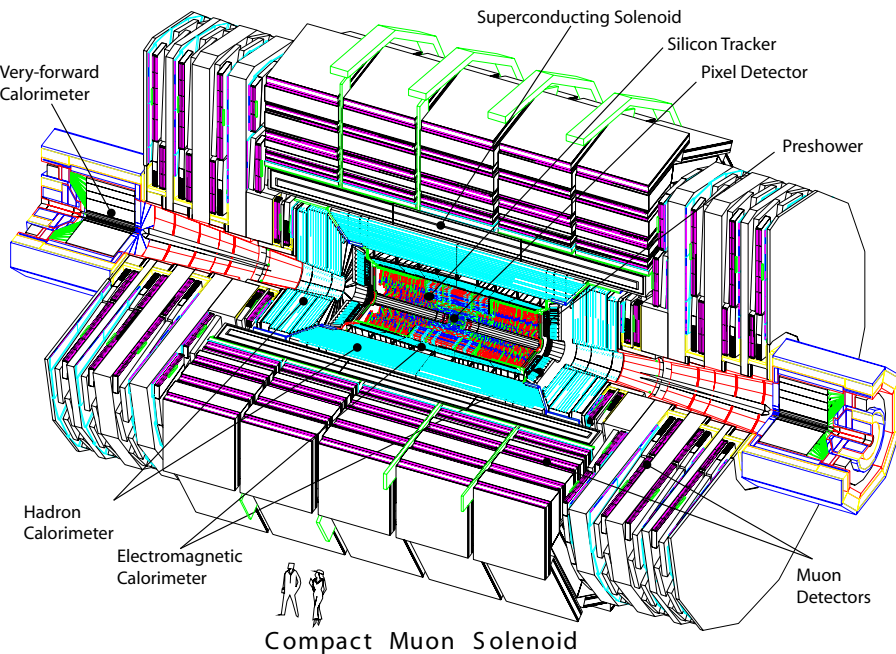


Figure 3.1: A drawing of the CMS detector. [27]

The goals for the CMS with respect to its purpose in the LHC programme is very good muon identification and good momentum resolution over wide range of phase space and ambiguous determination of muon charge. Very good inner tracking system for detection of charged parti-

cles and high efficiency offline b quark tagging and τ tagging. Other important requirements, specially for Higgs searches, is diphoton mass resolution, and photon and electron identification and isolation at high energies. CMS detector with its design meets all these requirements as it shown in following sections of this chapter. Each section describing a part of the detector separately together with it's role in CMS.

3.1 CMS coordinate system

CMS uses a right-handed coordinate system with the origin in the interaction point. z -axis is pointing along the beam line. x -axis is pointing towards the center of the ring while y axis points upwards. Two angles are used when describing position inside the detector, azimuthal angle ϕ and polar angle θ . ϕ angle lies in $x - y$ plane with a range $[-\pi, \pi]$ and is defined as $\phi = \text{atan}(y/x)$. The other angle θ is usually not used in high-energy physics because differences in θ are not Lorentz invariant. The variable that is Lorentz invariant is rapidity:

$$y = \frac{1}{2} \ln \left[\frac{E + p_z}{E - p_z} \right] \quad (3.1)$$

In high energy experiments in the relativistic limit where $E \gg m$, a quantity called pseudorapidity is a good approximation of rapidity:

$$\eta = -\ln \left[\tan \frac{\theta}{2} \right] \quad (3.2)$$

Pseudorapidity Lorentz invariance means that a measurement of $\Delta\eta$ between particles is not dependent on specifying a reference frame, such as the rest frame of a particle or the laboratory frame. When using the term "forward" direction, it refers to regions of the detector that are close to the beam axis, at high $|\eta|$. When the distinction between "forward" and "backward" is relevant, the former refers to the positive z -direction and the latter to the negative z -direction.

3.2 Solenoid magnet

Solenoid magnet within the CMS has the length of 12.9 m, an inner diameter of 5.9 m provides provides a magnetic field of 3.8 T. The solenoid is large enough to contain inner tracking system and calorimeters inside which reduces the material budget before the energy measurement in the calorimeters. The strong magnetic field increases the curvature of the trajectories of the highly energetic particles thus improving the momentum resolution.

Superconducting materials are used to build the solenoid with the operational temperature of 4.6 K. It is composed of four layers of superconducting material inserted in aluminum. Muon

detectors outside the solenoid operate in 2 T magnetic field enhanced by the 10 000-t iron yoke.

3.3 Inner tracker system

The role of inner tracking system in CMS is to provide a precise measurement of charged particles trajectories created in collisions with $p_T > 1$ GeV and the pseudorapidity $|\eta| < 2.5$. Other important task is precise secondary vertex positions reconstruction and impact parameter determination. The size of CMS inner tracker is 5.8 m in length with a diameter of 2.5 m. Large magnetic field of 4 T is provided by the surrounding solenoid and is homogeneous across the entire inner tracking system. With the design LHC luminosity, expected occupancy of inner tracking system is more than 1000 particles from 20 primary interactions in each bunch crossing. This requires high granularity detectors with fast responses and low dead time of the detector. Trying to design a detector with these characteristics while at the same time reducing the amount of material in the detector to minimum and taking into account the radiation hardness, lead to the solution of building an all-silicon detector. CMS inner tracking system has two separate parts, Pixel detector and Strip detector which are described below.

3.3.1 Pixel Detector

Pixel detector is the closest part of the CMS to the interaction point. Barrel pixel is the central part with three layers located at radii of 4.4 cm, 7.3 cm and 11 cm. On each side of the barrel pixel, there are two discs at $z = 34.5$ cm and 46.5 cm. The detector is fully modular hybrid detector with silicon layer bump bonded to read-out chips where each pixel is read out separately.

DODATI JOS O PIXELU

3.3.2 Strip detector

Silicon pixel tracker is built in layers around Pixel detector where track particle flux is lower and lower granularity detector can be used instead. Detector is built of strips in which a passing charged particle induces current. Current is then transferred to silicon detectors connected to the wires. The barrel section of the strip detector consists of four layers in the inner part (TIB) and 6 layer in the outer part (TOB). In the forward regions there are three tracker inner discs (TID) on each side of the barrel and 9 layers in the tracker endcap (TEC).

par Some strips are built in double layers tilted against each other by an angle of 100 mrad to precisely measure the position of both $r\phi$ and rz directions. The pitch size between strips varies from 80 μm in the TIB to 184 μm in TOB and TEC. With the increasing distance from the

interaction point, both strip pitch and strip length increase and sensor thickness becomes larger which affects the resolution.

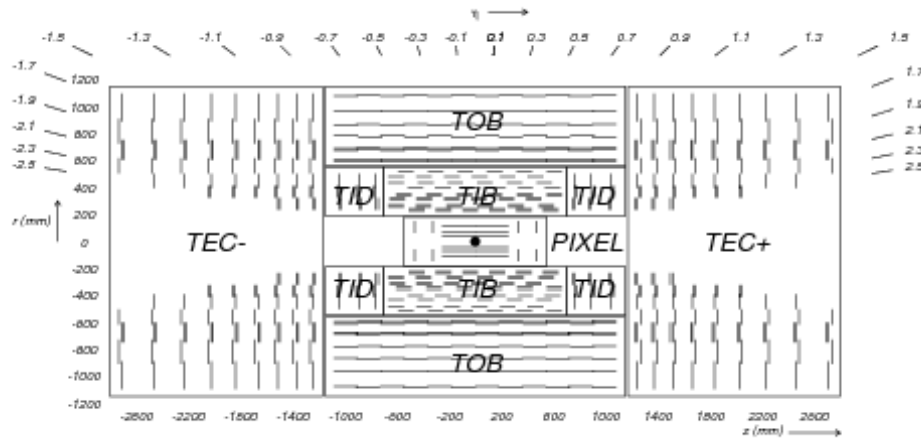


Figure 3.2: A drawing of the CMS strip detector. [27]

3.4 Electromagnetic calorimeter

The role of the Electromagnetic calorimeter in CMS is precise measurement of electron and photon energies and corresponding electromagnetic showers. It is built from lead tungstate (PbWO_4), a material with very high density (8.28 g/cm^3) and a small Moliere radius (0.89 cm) which is a scale of transverse dimension of the fully contained electromagnetic showers. The scintillation light emitted within a single bunch crossing of 25 ns is about 80% of the total light which is a large advantage of this material. The calorimeters is built of 61 200 crystals in the barrel region and 14 670 crystals in the endcaps. Each crystal has a size of $22 \times 22 \text{ mm}^2$ in the front, $26 \times 26 \text{ mm}^2$ at the back side and length on 23 cm in the barrel region. In the endcaps, the size of the crystals goes from 28.62×28.62 in the front to $30 \times 30 \text{ mm}^2$ in the back with a length of 22 cm. The whole systems covers the η range to $|\eta| < 3$.

Operation temperature of the detector is 18degC at which ~ 4.5 photoelectrons are collected per MeV. The blue-green scintillation light is measured my the avalanche photodiodes in the barrel and vacuum phototriodes in the endcaps.

The ECAL energy resolution is affected by three uncorrelated sources. Equation 3.3 shows the parametrisation of the ECAL resolution where parameters a , b and c are determined from the test beam. The stohastic term a is very low for the lead tungstate crystals ($a = 2.83 \pm 0.3\%$) which means that showers can be mostly contained within the crystals. The noise term b is determined from the electronics and is usually $b = 124 \text{ MeV}$. The last term c is the constant

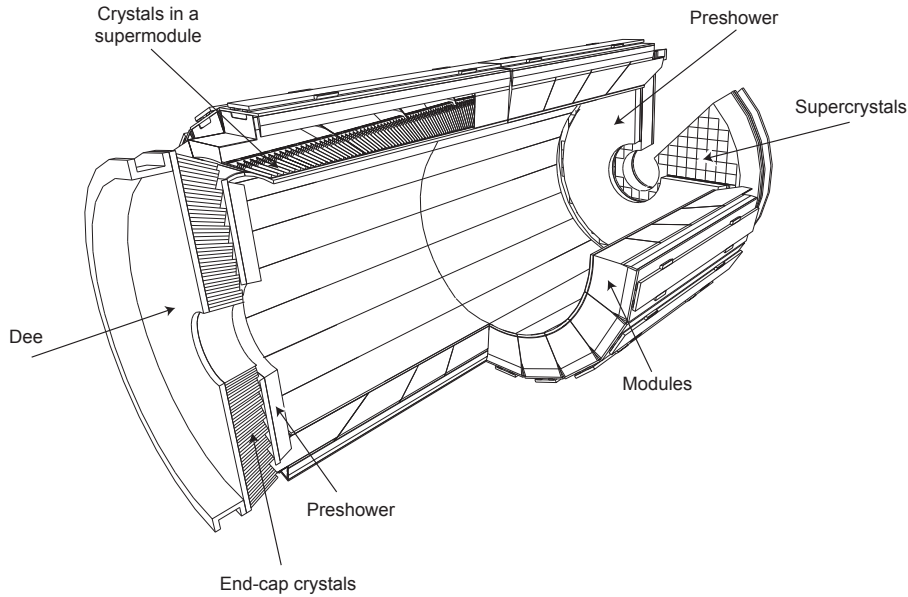


Figure 3.3: A drawing of the CMS electromagnetic calorimeter. [27]

term which limits the ECAL accuracy at high energies.

$$\left(\frac{\sigma_E}{E}\right)^2 = \left(\frac{a}{\sqrt{E}}\right)^2 + \left(\frac{b}{E}\right)^2 + c^2 \quad (3.3)$$

3.5 Hadronic calorimeter

Hadronic calorimeter is used to measure energies of hadrons like pions, kaons, protons neutrons etc. Barrel and endcap hadronic calorimeters cover the pseudorapidity range to $|\eta| = 3$. Since in the transverse direction, the absorber thickness is only 5.82 interaction lengths, additional layer was placed outside the solenoid. Hadronic calorimeter is a sampling calorimeter which consists of layers of brass and plastic scintillator layers. Showers are produced mostly in brass and are detected in the scintillator and reemitted in the narrow wavelength range in which photodetectors operate. In the endcap region, steel and quartz are used because of higher radiation hardness. There is an additional part of the detector placed 11.2 meters from the interaction point on both sides called forward HCAL which extends the coverage to $|\eta| = 5.2$. Large HCAL coverage and good energy measurement are very important for jet reconstruction as well as for missing transverse energy measurement.

3.6 Muon chambers

Muons are the only particles that pass the calorimeters and the solenoid and their charge and momentum is measured again in the outer part of the detector by the muon chambers. There are

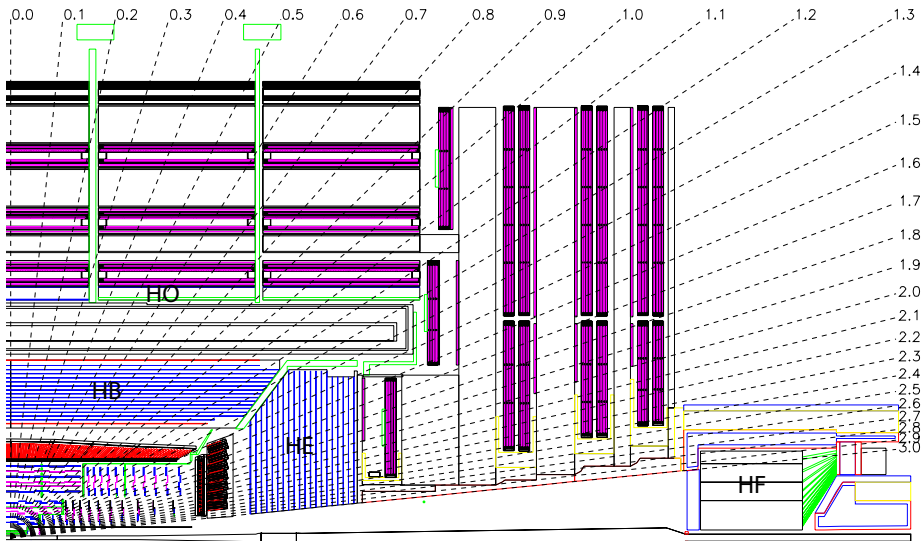


Figure 3.4: A drawing of the CMS Hadronic Calorimeter. [27]

three different types of the gaseous detectors used in the muon system, Drift tubes (DT), Resistive Plate Chambers (RPC) and Cathode Strip Chambers (CSC). Drift tubes are used in the barrel region where muon rate is relatively low and covers pseudorapidity range of $|\eta| < 1.2$. The signal in Drift tubes is generated when a particle ionizes the gas inside the tube and the charge is collected by wires which are at high voltages. Cathode Strip chambers are used in the endcap region where muon rate is much higher and magnetic field is not uniform. These are multi-wire proportional chambers with anodes that collect charge from the gas ionization. Resistive Plate Chambers are placed both in barrel and endcap region. These detectors are designed as two parallel plates which create a uniform electric field in the gas between them. The electrodes on the plates are highly resistive so that when charged particle passes, it causes an electron avalanche which passes through the plates and is collected by the external metallic strips. Their time resolution is of the order ~ 1 ns which makes RPCs a good choice for triggering although their spatial resolution is not so good.

Large magnetic field enables even for high p_T muons to be measured with a reasonable cell size in the muon chambers. The limiting factor for good resolution of low p_T muons in multiple scattering, and for high p_T muons the chamber resolution. The momentum resolution as a function of muon p_T is shown in Figure 3.6 and it shows both muon chambers resolution and inner tracker resolution together with the combined result.

3.7 Trigger

The design rate of the proton collisions at the LHC is 40 MHz, although during Run 1 data taking period, the rate was 20 MHz which corresponds to 50 ns bunch spacing. Data from

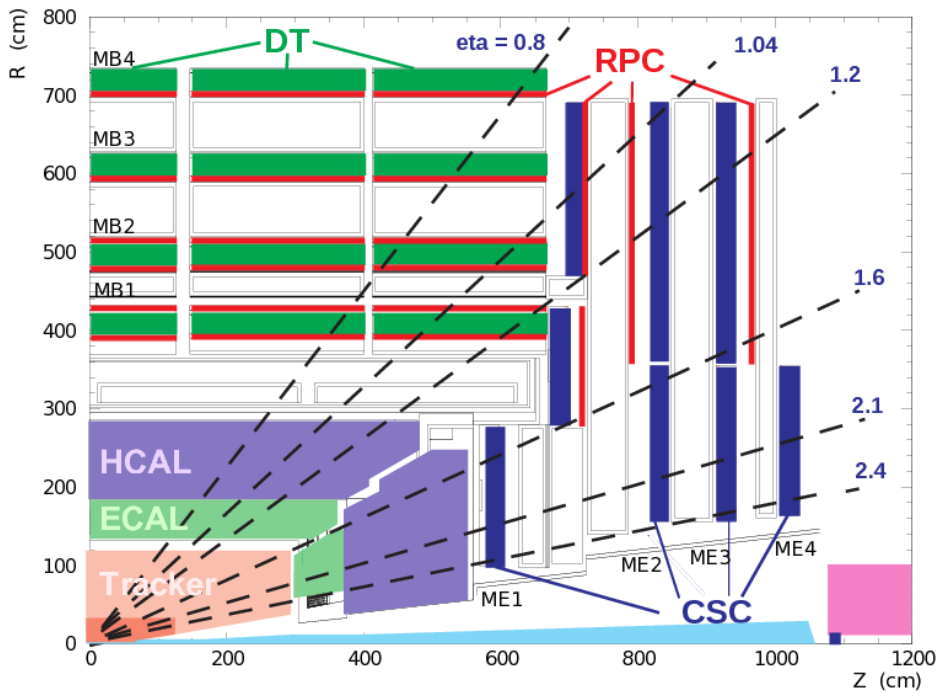


Figure 3.5: A drawing of the CMS muon chambers which consist of three different types of the detectors: DRift tubes, Cathode Strip Chambers and Resistive Plate chambers. [27]

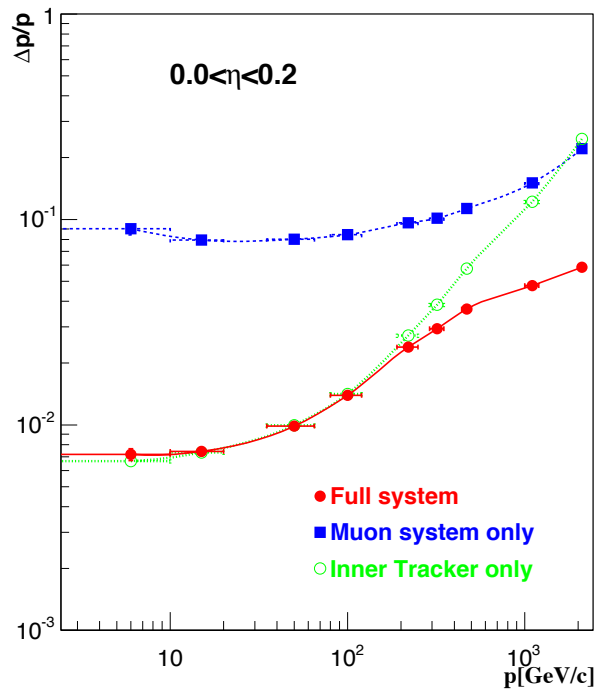


Figure 3.6: Muon resolution measurements for tracker, muon chambers and combined [27]

each of the bunch crossings is called an event. Since there are huge amounts of data coming from the subdetectors, it is necessary to apply some conditions which can reduce the rate to about 100 events per second. This is done by two level triggering system, first one called Level 1(L1) trigger and secong one called High Level Trigger(HLT). L1 trigger uses a special costum made electronics designed to reduce the output rate from 40 MHz to 100 kHz. Events which pass some loose criteria are than passed to the HLT. The L1 trigger uses the information from Calorimeters and Muon chambers to take the decision whether the event should be accepted or rejected usually searching fo presence of muons, jets above certain p_T , or looking at the total amount of E_T and E_T^{miss} . The time needed to send the signals to the electronics, run the L1 selection and send the information back to the subdetectors in $3.2 \mu\text{s}$. After L1 accepted the event, it is stored in the readout buffers where partial reconstruction takes place and the event is than processed by the HLT. This is a software farm which reduces the number of events to about 100 per second.

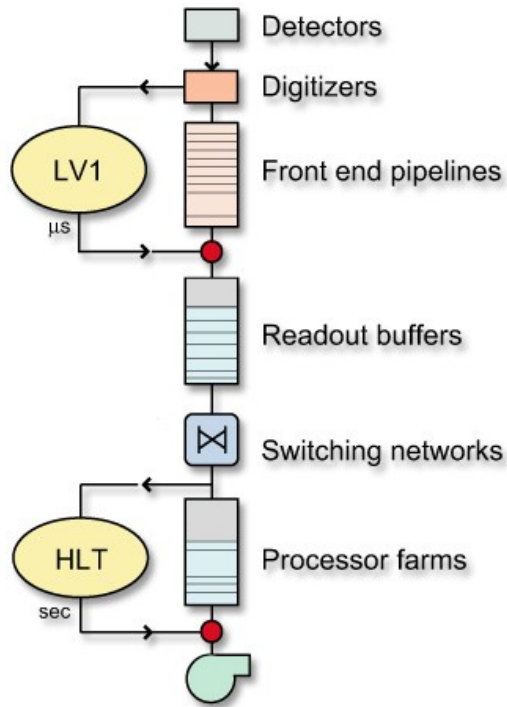


Figure 3.7: A drawing of CMS Trigger System. [27]

Chapter 4

Physics objects definitions

4.1 Electrons

Electrons in CMS are detected as a track in tracker and an energy deposit in the electromagnetic calorimeter. Two different algorithms are used for electron reconstruction, "tracker driven" seeding which is more suitable for low p_T electrons and electrons inside jets. Other algorithm is "ECAL driven" seeding which is optimized for high p_T isolated electrons. Both approaches take electromagnetic crystals with deposited energy and join them into *clusters*. Electron passing through the detector bends due to magnetic field and interacts with the detector material emitting *bremsstrahlung* photons. ECAL energy deposits from these photons are spread in ϕ direction in very narrow η range and combined with the existing cluster forming a *supercluster*. Trajectories are reconstructed using modeling of electron energy loss in detector material and fitted with a Gaussian Sum Filter(GSF)[33].

Matching ECAL superclusters and reconstructed tracks is where the two approaches differ. Tracker driven seeding uses track from the electromagnetic calorimeter and tries to match it with the supercluster in the ECAL. Each electron candidate has to pass various quality cuts in order to maximize the probability of the electron coming from the hard interaction, and reject electrons from jets or conversion. These selection cuts can be divided into three categories: identification, isolation and conversion cuts. Details on electron reconstruction and performance can be found in [34].

4.1.1 Electron identification

Electron identification procedure first focuses on good matching between reconstructed track and supercluster, by imposing cuts on angular distance $\Delta\eta$ and $\Delta\phi$ between the two. These variables are computed as absolute η and ϕ distance of the supercluster and electron track extrapolated to the ECAL surface. Cut is also imposed on $\sigma_{in\eta\eta}$ which describes a shower

shape spread in η direction. This variable is particularly discriminating against clusters coming from electrons and energy deposits from photons and fakes. Shower shape is defined as:

$$\sigma_{i\eta i\eta} = \sqrt{\frac{\sum_i^{5\times 5} w_i (\eta_i - \eta_{seed})^2 \times \Delta\eta_{xtal}^2}{\sum_i^{5\times 5}}} \quad (4.1)$$

where i is running over all crystals in 5×5 block around supercluster seed, $\eta_i - \eta_{seed}$ is the distance in number of crystals in η direction between i -th crystal in supercluster and seed crystal and $\Delta\eta_{xtal}^2$ is the average width of a single crystal. Each crystal is given a weight defined as $w_i = \max(0, 4.7 + \ln E_i / E_{5\times 5})$, where E_i is a single crystal energy, and $E_{5 \times 5}$ is the sum of energy deposits inside a 5×5 crystal block. The ratio between the energy deposits in the hadronic calorimeter and electromagnetic calorimeter for electrons is used to discard the events with significant hadron activity.

Electrons coming from converted photons are rejected by requiring a hit in every layer of the inner tracking system. Additionally, for each electron track a fit is performed trying to combine it with another electron track under the hypothesis that both electrons originated from converted photon. Electron is selected only if this probability is sufficiently small. Electron compatibility with the primary vertex is estimated by looking at the impact parameters in both xy and z planes. Due to the gap in the electromagnetic calorimeter in $1.4442 < \eta < 1.566$, all electrons which have a supercluster position reconstructed in this range are rejected. A full list of identification criteria is summarized in Table 4.1.

Table 4.1: A summary of electron identification criteria.

Variable	Barrel	Endcap
$\Delta\eta <$	0.004	0.005
$\Delta\phi <$	0.03	0.02
$\sigma_{i\eta i\eta} <$	0.01	0.03
$H/E <$	0.12	0.10
$d_{xy} <$	0.02 cm	0.02 cm
$d_z <$	0.1 cm	0.1 cm
$(1/E - 1/p) <$	0.05	0.05
Missing hits	0	1
Vertex Fit Probability	10^{-6}	10^{-6}

4.2 Muons

Muons in CMS are reconstructed by combining a reconstructed track inside the tracker (*tracker track*) and track in muon chambers (*standalone muon track*). Similar as with electrons, two approaches are used for combining these objects. *Global muon reconstruction* approach uses a standalone muon track in the muon chambers and tries to find a matching tracker track by combining parameters of two tracks by projecting it to the common surface. This *outside-in* approach uses Kalman filter technique [35] to combine these two objects. The second approach for muon reconstruction is *tracker muon reconstruction* which starts from tracks inside the tracker with $p_T > 0.5$ GeV/c and total momentum $p > 2.5$ GeV/c as potential muon candidates. Extrapolation is then performed to the muon chambers taking into account the magnetic field, Coulomb scattering in the material and other energy losses. *Tracker moun* is found if at least one muon segment matches the extrapolated track. The efficiency of the *Tracker muon* reconstruction is higher for low energy muons than the efficiency for the Global muons, because only a single muon segment in the muon chambers is required. For high energy muons where more there are more segments inside muon chambers, *Global muon* algorithm is designed to have high efficiency.

4.2.1 Muon identification

In this analysis *particle flow* muon identification selection is applied to the *global* muons. Selection is applied in order to minimize misidentification of charged hadrons as muons, maximize the efficiency of identification of muons inside jets and ensure good momentum measurement. Muons used in the analysis have $|\eta| < 2.1$ and transverse momentum $p_T < 30$ GeV with more than 5 hits in the inner tracker system and at least one hit in pixel detector. At least one good muon chamber hit in the *global muon* track fit is required to have $\chi^2/ndof < 10$, at least two segments in two different muon stations should be matched to a track in order to suppress muons from in-flight decays. Cosmic muons are rejected by applying cuts on the impact parameter with respect to the primary vertex of $|d_{xy}| < 0.2$ cm and $|d_z| < 0.5$ cm. Muon identification criteria is summarized in Table 4.2.

4.3 Lepton isolation

Leptons from W decays are in general expected to be well isolated. The degree of isolation is calculated using *particle flow* approach by summing the transverse momenta contributions of particles around the lepton inside a specific cone. All charged particles are considered as well as photons and neutral hadrons with $p_T > 0.5$ GeV. The cone used for determination of energy deposits is defined as $\Delta R = \sqrt{\Delta\phi^2 + \Delta\eta^2}$ around the lepton axis and isolation measure

Table 4.2: A summary of muon identification criteria.

Variable	Requirement
number of pixel hits >	0
number of inner tracker hits >	5
$\chi^2/ndof <$	10
number of muon hits >	0
chambers with matched segments >	1
$d_{xy} <$	0.2 cm
$d_z <$	0.5 cm

is defined as:

$$I_{PF}^{rel} = \frac{\sum p_T^{charged} + \max(0, \sum E_T^\gamma + \sum E_T^{neutral} - 0.5 \sum E_T^{PU})}{p_T^l} \quad (4.2)$$

where $p_T^{charged}$ is the sum of the momenta of charged hadrons and E_T^γ and $E_T^{neutral}$ are the sums of photon and neutral hadron momenta. E_T^{PU} is the sum of the pile-up transverse energies from neutral particles and is calculated as a sum of track transverse momenta not coming from the primary vertex inside the isolation cone. This is divided by the factor of 0.5 which corresponds approximately to the ratio of neutral to charged hadron production in the hadronization process of pile-up interactions. Selected muons are required to pass isolation cut $I_{rel}^{PF} < 0.12$ and in case of additional muon veto $I_{rel}^{rel} < 0.2$. Electron isolation is computed in the same way with cut of $I_{rel}^{PF} < 0.1$ for selected electrons and $I_{rel}^{PF} < 0.15$ for vetoed additional electrons.

4.4 Jets

In high energy physics, jet is a colimated group of hadrons which emerges as a result of quark or gluon fragmentation and hadronization process. Hadrons reconstructed in a particle detector need to be combined in order to form a jet and give information about the initial parton. A set of rules has to be created for how to group particles and how to assign momentum to the new jet. Usually this is done by summing the four-momentum of each particle in a jet.

4.4.1 Jet algorithms

Jet algorithms are taking into account the distance between particles and define rules which determine which particle belongs to which jet. Same jet algorithms should be applicable to both,

experimental data and theoretical calculation. Other important properties of jet algorithms is *infrared safety* and *collinear safety* which means is an event is modified by addition of soft emission or collinear splitting, the final number of hard jets will remain unchanged. These two properties together are called *IRC safety*. IRC unsafe jet algorithms may break the cancellation of divergences by yielding one set of jets for tree-level splitting while loop diagrams lead to another, as shown in figure 4.1, giving infinite cross-sections in the final calculations. Jet definitions, jet relation to partons and an overview of different jet algorithms are summarized in [36].

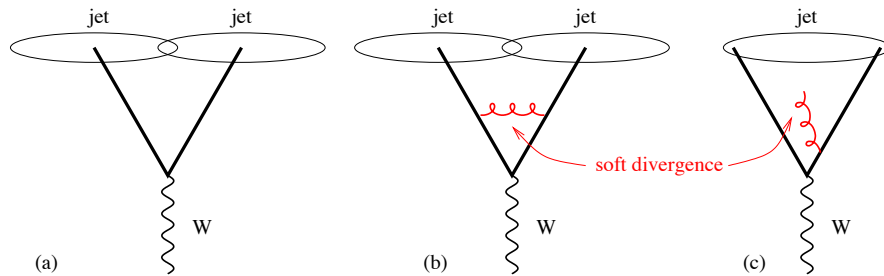


Figure 4.1: Configuration showing IC unsafety with W boson and two partons. Adding a soft gluon causes two jets to be reconstructed as one. [36]

There are two types of jet algorithms which are most commonly used: *cone algorithms* and *sequential recombination algorithms*. In the case of *cone algorithms*, a jet is defined as a set of particles inside a stable cone around their center of mass. Most popular cone algorithm is *iterative cones* (IC) where a seed particle is chosen and momenta of all particles around that initial particle inside a cone of radius R are summed. After adding each new particle to the sum, the direction of the new sum is taken as a seed direction, and the procedure repeats until the direction of the resulting cone is stable. Particles inside the cone are then removed from the list of available particles and the procedure repeats. This approach is not IRC safe as nearly collinear splitting of the hardest particle in the event can be reconstructed as two jets thus leaving another, less energetic, particle, pointing in another direction, to become the hardest particle in the event, yielding different set of jets. Cone algorithms can be IRC safe using a *seedless cone* (SC) algorithm where all stable cone solutions are identified at once. However this approach is very time consuming even for small number of particles and thus very impractical to use. In the *sequential recombination algorithms* at hadron colliders two longitudinally invariant distances are introduced: d_{ij} which is the distance between each pair of particles and d_{iB} which is the particle-beam distance. These distances are defined as:

$$d_{ij} = \min(k_{T,i}^{2p}, k_{T,j}^{2p}) \frac{\Delta R_{ij}^2}{R^2} \quad (4.3)$$

$$d_{iB} = k_{T,i}^2 p \quad (4.4)$$

where ΔR_{ij} denotes the distance in the $\eta - \phi$ plane and is computed as

$$\Delta R_{ij}^2 = (\eta_i - \eta_j)^2 + (\phi_i - \phi_j)^2$$

. R is an angular cut-off, similar to the one in *cone algorithms* and p defines which particles are clustered first which is described below. Both are free parameters of the algorithm. The algorithm is applied using the following approach: first two distances d_{ij} and d_{iB} are computed and minimal values are found. If d_{ij} is smaller, that two particles are combined, treated as a new particle and the distance with next particle in the list is computed. In case of d_{iB} being smaller, i is declared to be the final jet and removed from the list of particles. The procedure continues until there are no more particles in the list.

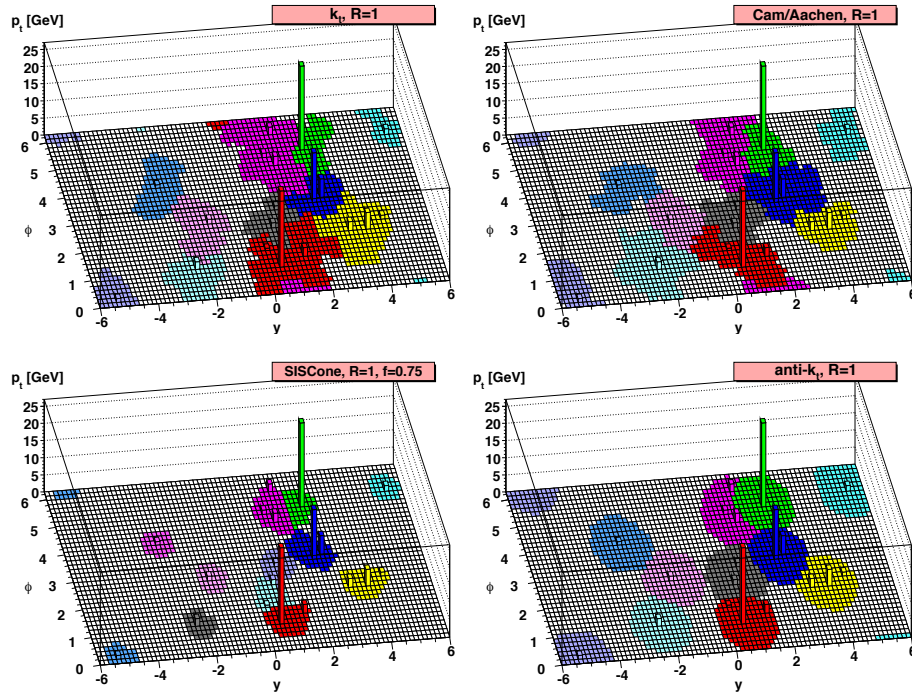


Figure 4.2: Clustering same set of reconstructed particles into jets using different jet algorithms. [36]

Parameter p defines which particles are clustered first thus defining the type of algorithm. The k_T algorithm uses $p = 1$, clustering soft particles first. This results in irregularly shaped jets, as shown in figure 4.2, which are sensitive to radiation in the event and difficult to calibrate. The *Cambridge-Aachen* algorithm (CA) uses $p = 0$ thus relying only on angular distribution of the input particles. This approach is particularly useful for jet substructure analysis and is less sensitive to radiation. The algorithm used in this analysis is *anti- k_T* algorithm where $p = -1$ clusterizing the hardest particles first [37]. *Anti- k_T* is an IRC safe algorithm with jets that are

circular in shape because they are not affected by the softer components of the jet.

4.4.2 Jet corrections

Measured jet energy at detector level in general doesn't correspond to the energy of the originating particle. Jet calibration procedure is introduced to compensate for the nonlinear response of the calorimeters. This is done using a factorized approach where corrections on each level of correction are determined separately as described in [38]. Final corrected jet momentum is obtained from measured p_T^{raw} according to:

$$p_T^{corr} = C_{offset}(p_T^{raw}, \eta) \times C_{rel}(\eta) \times C_{abs}(p_T') \times C_{res}(p_T'', \eta) \times p_T^{raw} \quad (4.5)$$

where offset correction C_{offset} and calibration factors C_{rel} and C_{abs} are applied to both data and simulation, C_{res} is applied only to data. Corrections are applied sequentially, in a fixed order such that $p_T' = C_{offset} \times C_{rel}(\eta) \times p_T^{raw}$, and $p_T'' = C_{rel}(\eta) \times C_{abs}(p_T')$. Correction factors used in this analysis can be found in [39]. Each level of corrections is summarized below:

- Offset correction C_{offset} compensates for energy contributions arising from pile-up events or instrument noise. The offset is determined in dependence of pseudorapidity, jet area $p_T density$ which is described in [40].
- Relative correction C_{rel} is aimed to flattening the jet scale in pseudorapidity. The correction is determined from simulation, adjusting the jet scale in all η regions to one of the jets in $|\eta| < 1.3$ without changing the absolute scale.
- Absolute correction C_{abs} flattens the jet scale in p_T . This correction is also determined from QCD multijet events as inverse of average response at fixed p_T^{gen} .
- Residual correction C_{res} is applied only to data in order to account for possible residual differences in data and simulation agreement after applying absolute and relative corrections. These corrections are derived using events with momentum balance in transverse plane, like dijet events or $Z/\gamma +$ jet events.

The total jet correction for a fixed jet p_T as a function of pseudorapidity is shown in figure 4.3.

4.4.3 Jet identification

This analysis uses $anti - k_T$ algorithm with cone size $R = 0.5$. Jet algorithm implementation is done in the *Fast-jet* package [41]. Depending on which signals is the algorithm applied to, there are different kinds of jets: calo jets (using calorimeter deposits), jet-plus-track jets (calorimeter deposits complemented with tracker information) and most widely used *particle flow* jets (PF). These jets are clustered from PF particles identified with PF algorithm, thus using the information not only from HCAL, but also from tracking system and ECAL which

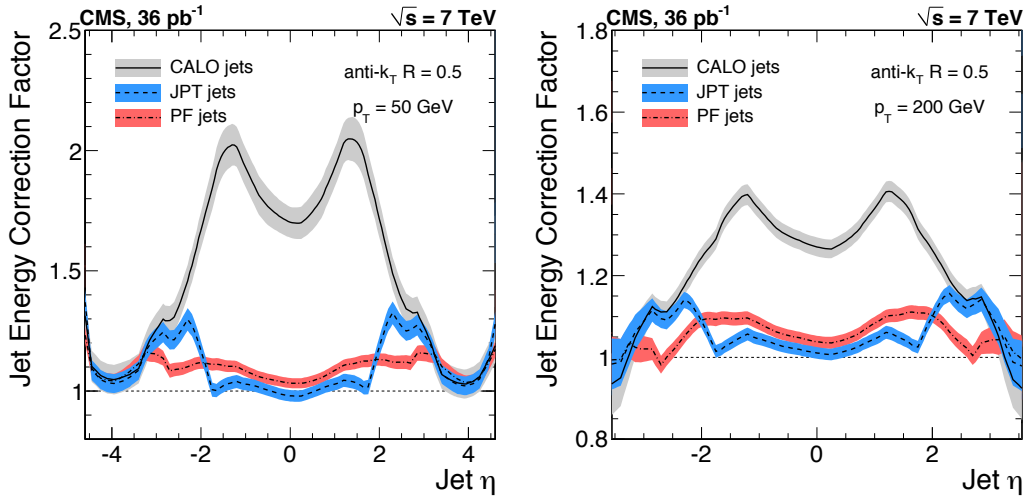


Figure 4.3: Total jet energy correction as a function of pseudorapidity of two different jet p_T values. Corrections are shown for all three types of jets, calo, JPT and PF jets. Bands indicate corresponding uncertainty.

show much better resolution. Only neutral fraction of the jet is measured only with HCAL which makes about 15% of the total jet composition. PF jets show excellent performance and are the default jets for most CMS analysis. Pile-up information is also taken into account by removing charged hadrons originating from pile-up vertices from the list of particles available for the jet clusterization. This procedure is called *charged hadron subtraction*. Some additional cuts to the jet composition are applied in order to endure good jet identification.

Table 4.3: A summary of jet identification criteria.

Variable	Requirement
Neutral hadron fraction	< 0.99
Neutral EM fraction	< 0.99
Number of Constituents	> 1
Additional cuts for $ \eta < 2.4$	
Charged hadron fraction	> 0
Charged multiplicity	> 0
Charged EM fraction	< 0.99

4.4.4 Jets from b quarks

Properties of the bottom quark, like relatively large mass and long lifetime, can be used to identify hadronic jets originating from b quarks. Such jets are originating from secondary inter-

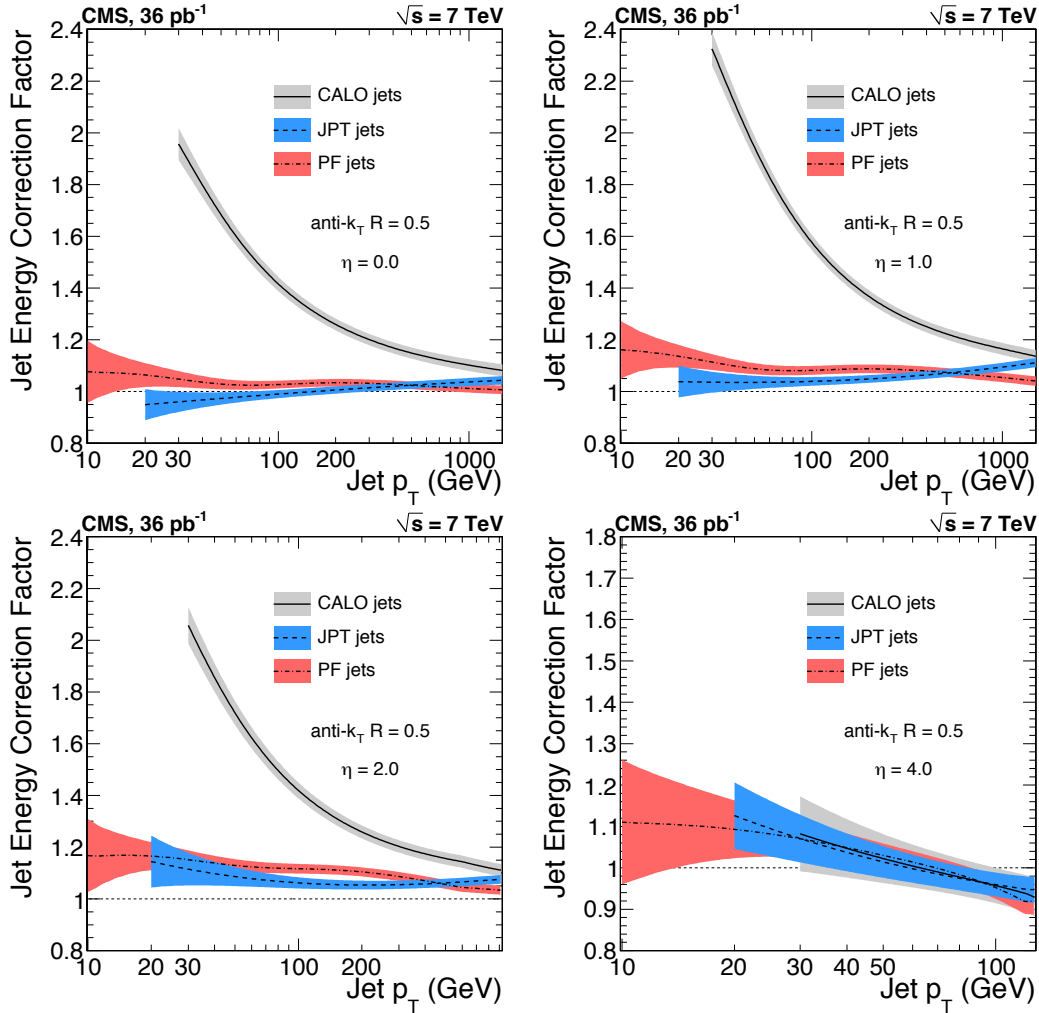


Figure 4.4: Total jet energy correction as a function of transverse momentum for four different η values. Corrections are shown for all three types of jets, calo, JPT and PF jets. Bands indicate corresponding uncertainty.

action point with significant impact parameter, and p_T of the jet constituents is harder than for light jets.

4.5 Missing transverse energy

Missing transverse momentum is the imbalance in the vectorial sum of transverse momenta of all measured particles. Momentum conservation delegates that the imbalance arises from weakly interacting neutral particles such as neutrinos. Missing transverse energy is the magnitude of the missing transverse momentum and is calculated as:

$$E_T^{miss} = \left| - \sum_i \vec{p}_i \right| \quad (4.6)$$

where i goes over all visible particles. Measurement of the missing transverse energy relies on the good measurement of all other particles in the event and as such is very sensitive to detector inefficiencies, particle missmeasurements, limited acceptance of the detector, cosmic-ray particles all of which can cause artificial missing energy. There are several approaches to determine E_T^{miss} . In this analysis, particle flow technique is used which tries to identify each particle each particle in the event by combining the information from all subdetectors and gives the best missing energy resolution.[42, 43] Several corrections are applied to the E_T^{miss} which include jet energy correction propagation, pile-up correction and phi modulation correction.

Chapter 5

Event selection and analysis strategy

Signal events are characterized by presence of a W boson and two jets which have been tagged as coming from b quarks. Candidates for a W boson are identified as isolated muons or electron and significant missing energy. Jets are identified as particle flow objects clustered with anti- k_T algorithm with a cone size of 0.5. Standard jet energy corrections and resolution smearing procedures prescribed by the Jet POG are applied. Combined secondary vertex (CSV) algorithm is then used to identify jets arising from fragmentation and hadronization of b-quarks. This algorithm combines in an optimal way information about track impact parameters and identified secondary vertices within the jet even when full vertex information is not available. Isolated leptons not arising from W decays are not expected, and additional jet activity is minimal.

5.0.1 Signal extraction

Signal event selection is described in the Signal selection section. For each of the major backgrounds a separate control region is defined in order to verify Monte Carlo normalizations.

The dominant backgrounds encountered in this analysis arise from few sources:

- **Top quarks:** production of $t\bar{t}$ pairs and single top represent a challenging background at the LHC because of their relatively large production cross sections. $t\bar{t}$ events are largely reduced by requiring an additional jet veto. Single top events are more difficult to reject relative to signal using just topological cuts, but production cross-section is smaller resulting in a smaller contribution in the final distributions.
- **W + light and c jets:** contribution from this source of background is largely reduced by applying b-tag requirement to selected jets.
- **Drell-Yan:** contribution from this process is largely reduced by requiring only one isolated lepton in the final state.
- **Dibosons(WW, WZ, ZZ):** contribution from this type of background in case where one boson decays leptonically and the other decays to jets is indistinguishable from the signal

events apart from the peak in the invariant mass distribution of two jets.

For this test $t\bar{t}$ multijet control region is used which is defined to be same as signal region, but requiring additional jet activity.

5.0.2 Systematics

The primary physics result described in this note is the cross section for production of a W boson and two b jets. Systematic uncertainties on the expected signal and background yields and shapes affect the final result. For a given systematic variation, a new set of signal and background templates was created which may differ both in shape and normalization from the original template. These shape variations are included in the final fit. Several sources of systematic variations have been considered:

- **Luminosity:** an uncertainty of 2.2% for luminosity measurement during 2012 datataking.
- **Jet energy scale:** the jet energy scale for each jet is varied within one standard deviation based on p_T and η , and the efficiency of the analysis selection is recomputed to assess the systematic variation on the normalization and shape of the signal and all background components.
- **Jet energy resolution:** we smear the energy resolution for each jet using the Jet- MET prescription as our default, and then modified signal and background templates are created in which jet energy is smeared by $\pm 1\sigma$ taken from JetMET POG.
- **Lepton energy scale:** muon and electron trigger, reconstruction, and identification efficiencies are determined in data using the standard tag-and-probe technique with Z bosons. The systematic uncertainty is evaluated by varying lepton energy scale for each lepton within one standard deviation taken from POG.
- **Unclustered missing energy:** we follow the suggested procedure from the JetMET POG to determine the systematic uncertainty on the calibration of unclustered MET (missing energy associated with particles not clustered into jets).
- **MC samples normalizations:** the finite size of the signal and background MC samples are included in the normalization uncertainties. Normalizations are also allowed to vary within the uncertainties of measured Standard model cross-sections.(cite all sources)
- **Jet b-tagging:** official b-tagging scale factors are applied consistently to jets in signal and background events.

Contributions from different sources of systematic variations are summarized in Table 5.1. Table also shows relative contribution to the signal strength uncertainty for each source of uncertainty together with the decrease in total systematic uncertainty when removing specific source of uncertainty.

Source	Type	Event yield uncertainty range (%)	Individual contribution to μ uncertainty (%)	Effect of removal on μ uncertainty (%)
b-tag efficiency	shape	10.34	1.48	1.73
b-tag fake rate	shape	0.08	0.01	0.40
Jet resolution	shape	0.01	0.02	0.52
Jet energy scale	shape	0.07	< 0.01	1.36
Unclustered MET	shape	< 0.01	< 0.01	5.20
Muon scale	shape	0.12	< 0.01	0.38
Luminosity	norm.	2.60	1.90	1.21
Monte Carlo statistics	norm.	0.78	2.40	5.83

Table 5.1: Information about each source of systematic uncertainty together with the information whether just normalization or shape is included in the final fit. The table also shows the uncertainty on signal and background yields and the relative contribution to the signal strength uncertainty. Due to correlations, the total systematic uncertainty is smaller than the quadrature sum of individual uncertainties. The last column shows the decrease in total systematic uncertainty when removing specific source of uncertainty.

5.0.3 Fit Results

Binned maximum likelihood fits are performed using templates derived from simulation. Systematic uncertainties on the fitted scale factors are determined by evaluating the effect on the template shapes from various sources of systematics, including b-tagging and jet energy scale and resolution. Final fit is performed simultaneously fitting transverse mass distributions in both signal region and $t\bar{t}$ multijet control region .

Final yields are summarized in the Tables 5.3 for signal region and 5.2 for $t\bar{t}$ multijet control region. Obtained yields are found to be in a good agreement with data. Measured signal strength for Wbb of $r = 1.34 \pm 0.16$ is in good agreement with signal strengths from Results section.

5.0.4 Tests of the fit stability

Additional tests were performed in order to verify the fit stability of the signal strength. This was done by fitting different combinations of distributions in both signal region and $t\bar{t}$ control region. Additional distributions include missing energy in the signal region and $t\bar{t}$ control region and invariant mass of third and fourth jet in $t\bar{t}$ control region. All distributions show good agreement in shapes between data and Monte Carlo. Fitting procedure is the same as described in section 5.0.3. Obtained signal strengths are summarized in Table 5.4.

W+bb		Fit Result: $r = 1.15 \pm 0.16$	
Sample	Prefit	Postfit	
W+bb	370.8 ± 12.3	556.6	
W+cc	20.3 ± 5.3	24.0	
W+udscg	1.7 ± 1.0	1.7	
Z+jets	21.8 ± 6.9	22.9	
Single Top	540.7 ± 14.2	624.5	
T \bar{T}	5577.3 ± 20.5	6383.7	
VV	25.3 ± 1.3	28.2	
QCD	234.4 ± 10.7	158.7	
Sum	6792.4 ± 31.1	7906.3	
Data		7995.0 ± 89.4	

Table 5.2: Data and MC yields before and after the fit in $t\bar{t}$ control region.

W+bb		Fit Result: $r = 1.34 \pm 0.16$	
Sample	Prefit	Postfit	
W+bb	879.7 ± 23.2	1350.0	
W+cc	35.5 ± 8.2	42.5	
W+udscg	19.7 ± 6.9	20.1	
Z+jets	122.5 ± 17.3	131.2	
Single Top	722.1 ± 15.5	833.0	
T \bar{T}	2338.6 ± 11.1	2676.7	
VV	106.4 ± 2.6	121.4	
QCD	249.3 ± 14.9	220.6	
Total MC	4473.9 ± 39.4	5426.1	
Data		5355.0 ± 73.2	

Table 5.3: Yields of MC samples before and after the fit.

Fitted distribution (Wbb/TT)	Signal Strength	Yield Ratio
M_T/M_T	1.34 ± 0.15	1.55
M_T/E_T^{miss}	1.31 ± 0.14	1.52
$M_T/M(j_3 j_4)$	1.35 ± 0.16	1.53
E_T^{miss}/M_T	1.43 ± 0.21	1.64
$E_T^{\text{miss}}/E_T^{\text{miss}}$	1.33 ± 0.17	1.53
$E_T^{\text{miss}}/M(j_3 j_4)$	1.38 ± 0.21	1.55

Table 5.4: Signal strengths obtained by fitting different distributions. Signal strengths are found to be consistent with each other.

Appendix A

Lorentz angle measurement in Pixel detector

Lorentz angle is measured by using grazing angle method described in detail in [44]. From the individual signals in the detector, using reconstruction algorithms, tracks of muon candidates are obtained. From these reconstructed track it is possible to extract the entry point (x_{reco}, y_{reco}) to each layer of the detector. Distance between reconstructed entry point and the actual hit in the detector is then defined as ($\Delta x, \Delta y$):

$$\Delta x = x_{center} - x_{reco} \quad (\text{A.1})$$

$$\Delta y = y_{center} - y_{reco} \quad (\text{A.2})$$

where (x_{center}, y_{center}) is the position of each individual pixel center in the observed cluster. Drift of the electrons can be determined using three impact angles defined in the following way:

$$\tan\alpha = \frac{p_z}{p_x} \quad (\text{A.3})$$

$$\tan\beta = \frac{p_z}{p_y} \quad (\text{A.4})$$

$$\tan\gamma = \frac{p_x}{p_y} \quad (\text{A.5})$$

where p_x, p_y and p_z are momentum components in local coordinate system which are calculated from reconstructed track parameters (Fig. A.1).

Drift of the electrons depends on the depth at which electrons are created. Depth of the electron

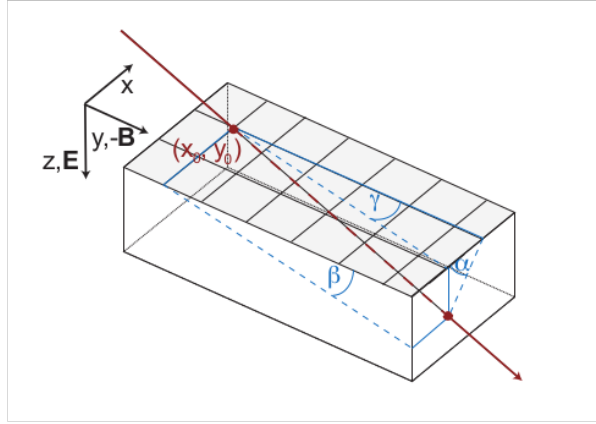


Figure A.1: Angle definitions for grazing angle method.

production z and drift due to magnetic field d are defined:

$$z = \Delta y \tan\beta \quad (\text{A.6})$$

$$d = \Delta x - \Delta y \tan\gamma \quad (\text{A.7})$$

This procedure is repeated for each pixel over many tracks in order to obtain charge drift distance vs depth. The Lorentz angle is the slope of this distribution. Without a magnetic field, the direction of the clusters largest extension is parallel to the track projection on the (x, y) plane. The average drift distance of an electron created at a certain depth is obtained from Fig. A.2. A linear fit is performed over the total depth of the detector excluding the first and last 50 μ where the charge drift is systematically displaced by the finite size of the pixel cell (Fig:A.3).

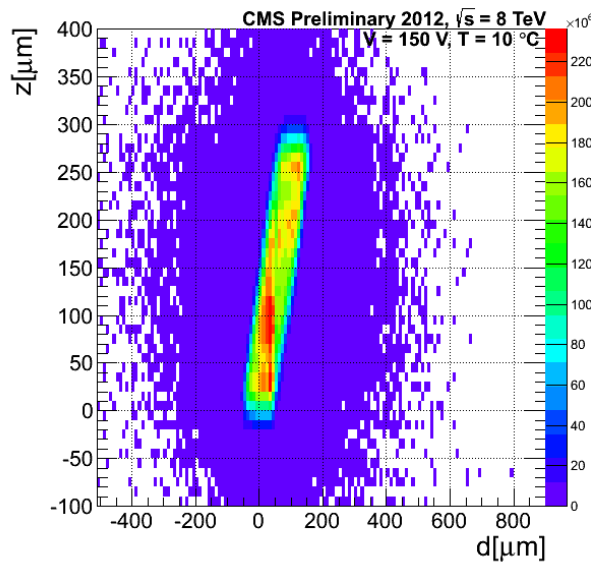


Figure A.2: Depth at which electrons in silicon bulk were produced as a function of Lorentz drift.

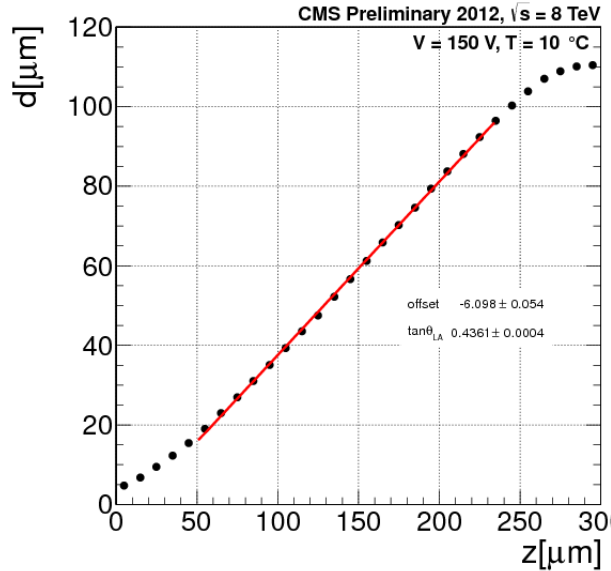


Figure A.3: The average drift of electrons as a function of the production depth. Slope of the linear fit result is the $\tan\theta_L$.

In order to obtain a good measurement, it is important to use clean tracks. Therefore, it required to have a well reconstructed muon tracks with $p_T > 3\text{GeV}$ and $\chi^2/\text{ndof} < 2$ which are required to have shallow impact angle with respect to local y direction with cluster size of at least 4 pixels in this direction. Summary of the selection criteria can be found in table A.1.

Table A.1: Selection criteria for Lorentz angle measurement

Cluster size in y	> 3
Track p_t	$> 3\text{GeV}/c$
χ^2/ndof	< 2
Hit residuals	$< 50\mu\text{m}$
Cluster charge	$< 120000\text{e}$

Figure A.4 shows how Lorentz angle changes with integrated luminosity. Results are shown for 23fb^{-1} of delivered luminosity in 2012. Increase in Lorentz angle measured with grazing angle method has been observed in all layers, with largest effect (6%) visible in layer 1 over this period of data taking.

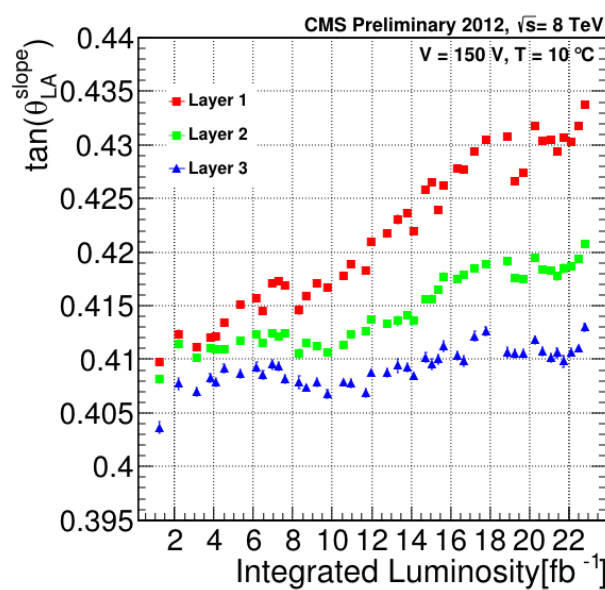


Figure A.4: Lorentz angle as a function of integrated luminosity for 2012.

Bibliography

- [1] Georges Aad et al. Observation of a new particle in the search for the Standard Model Higgs boson with the ATLAS detector at the LHC. *Phys.Lett.*, B716:1–29, 2012.
- [2] Serguei Chatrchyan et al. Observation of a new boson at a mass of 125 GeV with the CMS experiment at the LHC. *Phys.Lett.*, B716:30–61, 2012.
- [3] D. Griffiths. *Introduction to Elementary Particles*. John Wiley & Sons, New York, USA, 1987.
- [4] Makoto Kobayashi and Toshihide Maskawa. CP Violation in the Renormalizable Theory of Weak Interaction. *Prog.Theor.Phys.*, 49:652–657, 1973.
- [5] S. W. Herb, D. C. Hom, L. M. Lederman, J. C. Sens, H. D. Snyder, J. K. Yoh, J. A. Appel, B. C. Brown, C. N. Brown, W. R. Innes, K. Ueno, T. Yamanouchi, A. S. Ito, H. Jöstlein, D. M. Kaplan, and R. D. Kephart. Observation of a dimuon resonance at 9.5 gev in 400-gev proton-nucleus collisions. *Phys. Rev. Lett.*, 39:252–255, Aug 1977.
- [6] G. Arnison et al. Experimental Observation of Isolated Large Transverse Energy Electrons with Associated Missing Energy at $s^{**}(1/2) = 540\text{-GeV}$. *Phys.Lett.*, B122:103–116, 1983.
- [7] M. Banner et al. Observation of Single Isolated Electrons of High Transverse Momentum in Events with Missing Transverse Energy at the CERN anti-p p Collider. *Phys.Lett.*, B122:476–485, 1983.
- [8] John M. Campbell. Overview of the theory of W/Z + jets and heavy flavor. 2008.
- [9] Michelangelo L. Mangano. Production of W plus heavy quark pairs in hadronic collisions. *Nucl.Phys.*, B405:536–554, 1993.
- [10] Serguei Chatrchyan et al. Search for the standard model Higgs boson produced in association with a W or a Z boson and decaying to bottom quarks. *Phys.Rev.*, D89(1):012003, 2014.
- [11] Serguei Chatrchyan et al. Evidence for the direct decay of the 125 GeV Higgs boson to fermions. *Nature Phys.*, 10:557–560, 2014.

Bibliography

- [12] K.A. Olive et al. Review of Particle Physics. *Chin.Phys.*, C38:090001, 2014.
- [13] John M. Campbell, J.W. Huston, and W.J. Stirling. Hard Interactions of Quarks and Gluons: A Primer for LHC Physics. *Rept.Prog.Phys.*, 70:89, 2007.
- [14] A.D. Martin, W.J. Stirling, R.S. Thorne, and G. Watt. Parton distributions for the LHC. *Eur.Phys.J.*, C63:189–285, 2009.
- [15] Fabio Maltoni, Giovanni Ridolfi, and Maria Ubiali. b-initiated processes at the LHC: a reappraisal. *JHEP*, 1207:022, 2012.
- [16] R. Keith Ellis and Sinisa Veseli. Strong radiative corrections to W b anti-b production in p anti-p collisions. *Phys.Rev.*, D60:011501, 1999.
- [17] Michelangelo L. Mangano, Mauro Moretti, and Roberto Pittau. Multijet matrix elements and shower evolution in hadronic collisions: $Wb\bar{b} + n$ jets as a case study. *Nucl.Phys.*, B632:343–362, 2002.
- [18] F. Febres Cordero, L. Reina, and D. Wackerlo. NLO QCD corrections to W boson production with a massive b-quark jet pair at the Tevatron p anti-p collider. *Phys.Rev.*, D74:034007, 2006.
- [19] Seth Quackenbush, Edmond L. Berger, C.B. Jackson, and Gabe Shaughnessy. LHC Sensitivity to $Wb\bar{b}$ Production via Double Parton Scattering. 2011.
- [20] Jonathan R. Gaunt and W. James Stirling. Double Parton Distributions Incorporating Perturbative QCD Evolution and Momentum and Quark Number Sum Rules. *JHEP*, 1003:005, 2010.
- [21] Sunil Bansal, Paolo Bartalini, Boris Blok, Diego Ciangottini, Markus Diehl, et al. Progress in Double Parton Scattering Studies. 2014.
- [22] Serguei Chatrchyan et al. Study of double parton scattering using W + 2-jet events in proton-proton collisions at $\sqrt{s} = 7$ TeV. *JHEP*, 1403:032, 2014.
- [23] Serguei Chatrchyan et al. Measurement of the production cross section for a W boson and two b jets in pp collisions at $\sqrt{s}=7$ TeV. *Phys.Lett.*, B735:204–225, 2014.
- [24] T. Aaltonen et al. First Measurement of the b-jet Cross Section in Events with a W Boson in p anti-p Collisions at $s^{**}(1/2) = 1.96$ -TeV. *Phys.Rev.Lett.*, 104:131801, 2010.
- [25] V.M. Abazov et al. Measurement of the $p\bar{p} \rightarrow W + b + X$ production cross section at $\sqrt{s} = 1.96$ TeV. *Phys.Lett.*, B718:1314–1320, 2013.

Bibliography

- [26] Georges Aad et al. Measurement of the cross-section for W boson production in association with b-jets in pp collisions at $\sqrt{s} = 7$ TeV with the ATLAS detector. *JHEP*, 1306:084, 2013.
- [27] S. Chatrchyan et al. The CMS experiment at the CERN LHC. *JINST*, 3:S08004, 2008.
- [28] G. Aad et al. The ATLAS Experiment at the CERN Large Hadron Collider. *JINST*, 3:S08003, 2008.
- [29] K. Aamodt et al. The ALICE experiment at the CERN LHC. *JINST*, 3:S08002, 2008.
- [30] Jr. Alves, A. Augusto et al. The LHCb Detector at the LHC. *JINST*, 3:S08005, 2008.
- [31] Lyndon Evans and Philip Bryant. LHC Machine. *JINST*, 3:S08001, 2008.
- [32] Oliver Sim Brüning, Paul Collier, P Lebrun, Stephen Myers, Ranko Ostojic, John Poole, and Paul Proudlock. *LHC Design Report*. CERN, Geneva, 2004.
- [33] W. Adam, R. Frühwirth, A. Strandlie, and T. Todorov. RESEARCH NOTE FROM COLLABORATION: Reconstruction of electrons with the Gaussian-sum filter in the CMS tracker at the LHC. *Journal of Physics G Nuclear Physics*, 31:9, September 2005.
- [34] Electron reconstruction and identification at $\sqrt{s} = 7$ TeV. 2010.
- [35] R. Frühwirth. Application of kalman filtering to track and vertex fitting. *Nuclear Instruments and Methods in Physics Research Section A: Accelerators, Spectrometers, Detectors and Associated Equipment*, 262(2–3):444 – 450, 1987.
- [36] Gavin P. Salam. Towards Jetography. *Eur.Phys.J.*, C67:637–686, 2010.
- [37] Matteo Cacciari, Gavin P. Salam, and Gregory Soyez. The Anti-k(t) jet clustering algorithm. *JHEP*, 0804:063, 2008.
- [38] Serguei Chatrchyan et al. Determination of Jet Energy Calibration and Transverse Momentum Resolution in CMS. *JINST*, 6:P11002, 2011.
- [39] 8 TeV Jet Energy Corrections and Uncertainties based on 19.8 fb^{-1} of data in CMS. Oct 2013.
- [40] Matteo Cacciari and Gavin P. Salam. Pileup subtraction using jet areas. *Physics Letters B*, 659(1–2):119 – 126, 2008.
- [41] Matteo Cacciari, Gavin P. Salam, and Gregory Soyez. FastJet User Manual. *Eur.Phys.J.*, C72:1896, 2012.

Bibliography

- [42] Particle-Flow Event Reconstruction in CMS and Performance for Jets, Taus, and MET. Technical Report CMS-PAS-PFT-09-001, CERN, 2009. Geneva, Apr 2009.
- [43] Serguei Chatrchyan et al. Missing transverse energy performance of the CMS detector. *JINST*, 6:P09001, 2011.
- [44] B Henrich and R Kaufmann. Lorentz-angle in irradiated silicon. *Nucl. Instrum. Methods Phys. Res., A*, 477(1-3):304–307, 2002.